Characterization and analysis of the interlaminar behavior of thermoplastic composites considering fiber bridging and R-curve effects

Tijs, B. H.A.H.; Abdel-Monsef, S.; Renart, J.; Turon, A.; Bisagni, C.

DOI
10.1016/j.compositesa.2022.107101

Publication date
2022

Document Version
Final published version

Published in
Composites Part A: Applied Science and Manufacturing

Citation (APA)
Tijs, B. H. A. H., Abdel-Monsef, S., Renart, J., Turon, A., & Bisagni, C. (2022). Characterization and analysis of the interlaminar behavior of thermoplastic composites considering fiber bridging and R-curve effects. *Composites Part A: Applied Science and Manufacturing*, *162*, Article 107101. https://doi.org/10.1016/j.compositesa.2022.107101

Composites: Part A 162 (2022) 107101

Contents lists available at ScienceDirect

Composites Part A

journal homepage: www.elsevier.com/locate/compositesa

Characterization and analysis of the interlaminar behavior of thermoplastic composites considering fiber bridging and R-curve effects

B.H.A.H. Tijs [a,c,*], S. Abdel-Monsef [b], J. Renart [b], A. Turon [b], C. Bisagni [c]

[a] Fokker/GKN Aerospace, Papendrecht, The Netherlands
[b] University of Girona, AMADE, Polytechnic School, Girona, Spain
[c] Delft University of Technology, Faculty of Aerospace Engineering, Delft, The Netherlands

ARTICLE INFO

Keywords:
Thermoplastic composites
Interlaminar fracture
Cohesive law
Finite element analysis
Fiber bridging
R-curve effect

ABSTRACT

Thermoplastic composites can enable the development of new manufacturing techniques to make the aviation industry more sustainable while at the same time greatly benefit cost-efficient and high-volume production. One of the thermoplastic composite materials that can enable this transition is AS4D/PEKK-FC. In this work, the interlaminar properties of AS4D/PEKK-FC thermoplastic composite are characterized and analyzed by means of Mode I, II and Mixed Mode I/II at 50:50 tests, while considering fiber bridging and R-curve effects. In order to achieve stable crack propagation the test configurations are adjusted to account for the large fracture process zone ahead of the crack tip and an appropriate data reduction method is selected. The experimental data is reduced using an inverse methodology to extract cohesive laws based on only the load–displacement curves. Additionally, the use of this methodology provides new insights into the validity of two different mode II tests and the influence of fiber bridging on the mixed-mode interlaminar behavior. The interlaminar damage mechanisms are investigated by means of scanning electron microscopy. The resulting cohesive laws are implemented in commercial finite element software in tabular form, without the need for user-subroutines. All experimental test configurations are analyzed using a single material card and it is shown that fiber bridging and R-curve effects are well captured.

1. Introduction

There is a strong push in the aviation sector to move towards more sustainable and affordable aircraft structures. In order to meet these new requirements, it is inevitable that changes have to be made in the way aircraft structures are designed and manufactured. One of the materials that can facilitate this transition, is thermoplastic composite. Among many other benefits, the material offers improved mechanical properties, 'unlimited' shell life and also recyclability. Furthermore, thermoplastic composites also enable the use of new assembly techniques such as autoclave co-consolidation, out-of-autoclave and welding [1] which can greatly benefit cost-efficient and high-volume manufacturing. These new assembly techniques take advantage of the improved interlaminar mechanical properties compared to thermoset composites and can greatly reduce the amount of mechanical fasteners required. One of the most recent advancements that leverages this new technology, is the development of the next generation of thermoplastic composite aircraft fuselage [2]. This new fuselage design considers, among other materials, the fast-crystalizing Poly(Ether-Ketone-Ketone) thermoplastic polymer, also referred to as PEKK-FC [3]. In contrast to thermoplastic composites which have been studied in the past [4–9], PEKK-FC composites offer faster processing times due to the increased rate of crystallization and can thus make a significant impact in how aircraft structures are designed and manufactured [10]. What makes PEKK unique among the other high performance polymers in the PAEK family, is the ability to synthesize isomeric copolymers to lower the melting temperature well below polymer degradation and significantly widen the melt processing window [11]. However, there is currently not much experimental understanding of the failure mechanisms of this material and the availability of accurate experimental data and validated testing or analysis techniques is rather limited [3,12–15]. Additionally, achieving predictable crack growth under both static and cyclic loading conditions is of high importance in aircraft design. It is expected that the superior mechanical performance of thermoplastic composites compared to thermoset composites may be attributed to effects such as plasticity and fiber-bridging. These effects are known [16,17] to increase the size of the fracture process zone ahead of the crack-tip [18]. This large zone of damaged material makes it difficult to identify the exact position of the crack-tip, and thus makes the use of

* Corresponding author at: Fokker/GKN Aerospace and Delft University of Technology, The Netherlands.
E-mail address: bas.tijs@fokker.com (B.H.A.H. Tijs).

https://doi.org/10.1016/j.compositesa.2022.107101
Received 19 April 2022; Received in revised form 8 July 2022; Accepted 18 July 2022
Available online 22 July 2022

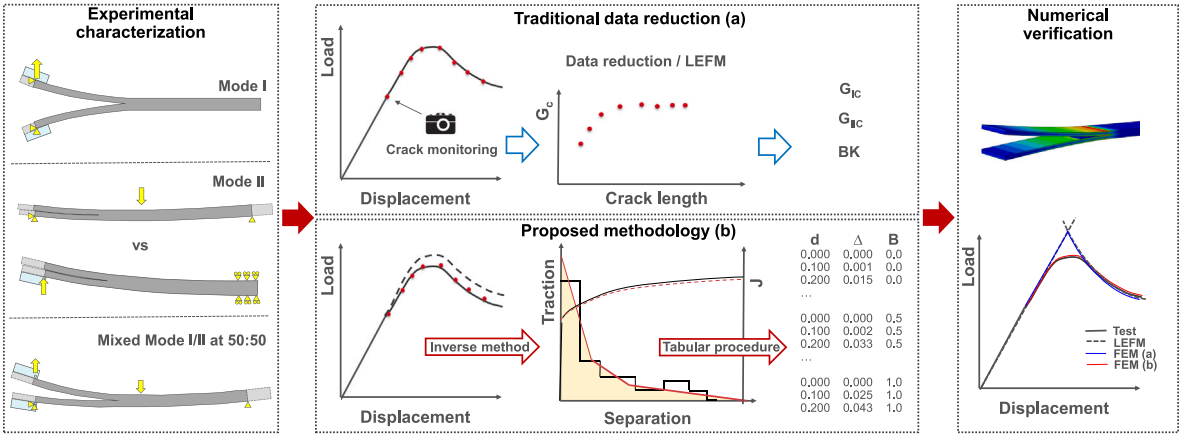

Fig. 1. Overview of the methodology.

traditional experimental data reduction methods, which rely on accurately monitoring the crack-tip, rather difficult [19]. Furthermore, in the End Notched Flexure (ENF) and Mixed-Mode Bending (MMB) test, where only limited room for crack propagation is available, the large fracture process zone may reach the load-introduction point before stable crack growth can be achieved [18].

The use of cohesive zone models has become a popular methodology to accurately simulate delamination growth in composites [20]. This model describes the failure during delamination in terms of tractions and displacements of crack opening. The model reduces the stiffness of the cohesive zone once damage is initiated, thus decreasing the traction while respecting the amount of fracture energy that is dissipated. The shape of this softening behavior can be described by a cohesive law, which can have many different forms (e.g. linear, exponential, bilinear, trapezoidal, parabolic and multilinear) [21,22], depending on the material behavior. This can for example be achieved by superposition of cohesive elements [23] in order to capture specific failure modes such as fiber bridging [24,25] or the influence of different ply interface angles [26]. However, this may not be so straight forward for mixed-mode cohesive laws [27] and accurately following the load–displacement curve remains difficult if there is a strong R-curve effect that requires an accurate description of the cohesive law [24].

The aim of this work is to characterize and analyze the interlaminar behavior of thermoplastic composites during quasi-static loading, while considering fiber bridging and R-curve effects. This covers the whole process from experimental characterization, fractographic investigation, data reduction, numerical implementation and verification by numerical analysis in a commercial finite element software.

2. Methodology

An overview of the methodology is shown in Fig. 1. First, the interlaminar fracture toughness is characterized in Mode I, II and Mixed Mode I/II at 50:50 on the Double Cantilever Beam (DCB) [28], End-Notched Flexure (ENF) [29], Calibrated End Loaded Split (CELS) [30] and Mixed-Mode Bending 50% (MMB50) [31] test configurations. The ENF and MMB50 test configurations are designed to achieve stable crack propagation, while accounting for the large fracture process zone of the thermoplastic material. Therefore, the validity of the mode II test method is investigated on both the ENF and CELS test and resulting interlaminar properties are compared.

The presence of the fracture process zone also influences the data reduction and analysis methodology. Consequently, both the traditional (Fig. 1a) and a proposed methodology (Fig. 1b) for experimental data reduction are considered. The traditional data reduction methods are based on the analytical Linear Elastic Fracture Mechanics (LEFM) solutions and require accurate measurement or estimation of the crack length. This results in an R-curve, which plots the calculated fracture toughness (G_c) against the crack length. The R-curve is however not a material property and depends on the test configuration, which means that the R-curve cannot directly be used in finite element analysis. Therefore, typically only the initiation or propagation fracture toughness is used. This makes the analysis conservative for large cracks when initiation values are used and unconservative and inaccurate for small crack propagation when propagation values are used.

The proposed methodology (Fig. 1b) makes use of an inverse data reduction method based on only the load–displacement curve [32,33]. This method extracts a step-wise representation of the cohesive law, which needs to be processed before it can be reliably used in finite element software. This is achieved through the use of a new procedure, which can ensure an accurate description of the shape of the cohesive law in tabular format. The benefit is that the full R-curve effect can be accounted for and user-subroutines are no longer required. The data reduction technique also provides new insights into how fiber bridging affects the mixed-mode interlaminar behavior of thermoplastic composites. Finally, numerical analyses are performed for all test configurations to verify the derived interlaminar properties and analysis methodology.

2.1. Material properties

The thermoplastic composite used in this work is the Solvay APC (PEKK-FC) thermoplastic polymer prepreg [3]. The prepreg is reinforced with the continuous unidirectional AS4D fiber with a nominal ply thickness of 0.14 mm. The laminates are manufactured by means of autoclave consolidation, where a process cycle is used that is representative for large aeronautical parts. This means a constant phase of at least 45 min and a cooldown speed in the order of 5 °C/min. The full set of material properties are provided in [15] and the relevant properties that are used in the data reduction and analyses of this paper are summarized in Table 1. All values are valid at room temperature ambient conditions. The Young's modulus is given in both tensile and compressive direction. The values of the Matrix 0.2% and 0.5% offset shear strength are estimated by the nonlinear shear parameters and equations provided in [15].

2.2. Specimen design

The specimen design is the same for all interlaminar tests and the specimens are machined from a single AS4D/PEKK-FC laminate that consists of 30 unidirectional plies. The specimens are designed to be 25 mm wide and 225 mm long. The benefit of this specimen design with increased length is, that during the start of the test campaign, both the mode I and II fracture toughness can be tested on a single specimen. This can be helpful for characterization of materials

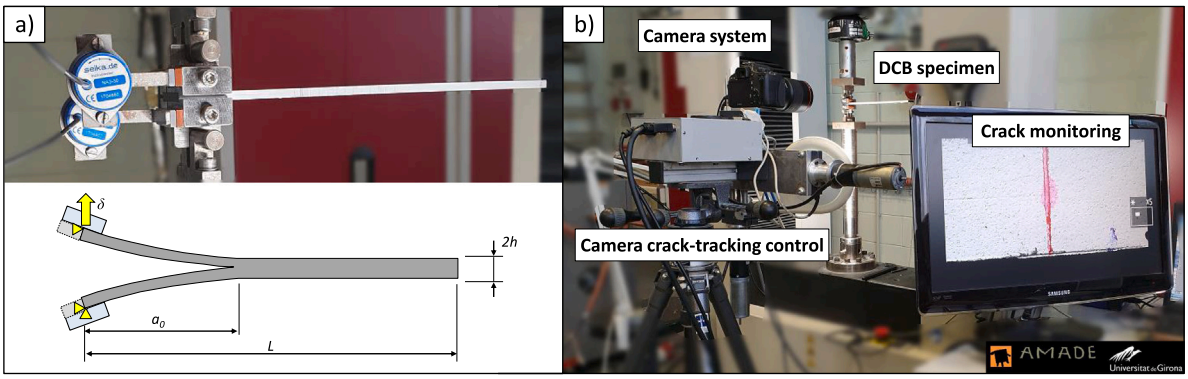

Fig. 2. DCB test setup at UdG AMADE lab: (a) DCB test configuration and geometrical parameters; (b) Test setup with camera and control system for crack monitoring.

Table 1
AS4D/PEKK-FC thermoplastic composite properties [15].

Property	Description	Value	Unit
E_{1t}	Young's modulus, longitudinal tensile direction	138 300	MPa
E_{1c}	Young's modulus, longitudinal compressive direction	128 000	MPa
E_{2t}	Young's modulus, transverse tensile direction	10 400	MPa
E_{2c}	Young's modulus, transverse compressive direction	11 500	MPa
$G_{12} = G_{13}$	Shear modulus	5190	MPa
ν_{12}	Poisson ratio, 1–2 direction	0.316	–
ν_{23}	Poisson ratio, 2–3 direction	0.487	–
Y_T	Matrix tensile strength	87	MPa
$S_{L_{0.2\%}}$	Matrix 0.2% offset shear strength (estimated)	50	MPa
$S_{L_{0.5\%}}$	Matrix 0.5% offset shear strength (estimated)	60	MPa
$S_{L_{5\%}}$	Matrix 5% offset shear strength	90	MPa

of which the fracture properties are not yet known. Without good estimations of the fracture properties, it may be difficult to set the correct initial crack length or span during these tests to achieve stable crack propagation. Furthermore, it also allows for some flexibility in testing higher toughness materials that may require a large span or clamping length during mode II and mixed-mode testing. However, for the actual propagation tests, it is recommended to only perform a small pre-crack to ensure that the crack front remains straight and without a fully developed fracture process zone. Due to the high processing temperature (377 °C, [3]) of thermoplastic composites, a 12.5 μm thick UPILEX foil is used as insert to start the crack. The length of this insert is 60 mm. The UPILEX foil is pre-treated with Frekote 700NC release agent to prevent contamination and allows for easy removal prior to testing. The benefit of this approach is that a single insert with a very small thickness can be used, thus guaranteeing a sharp as possible initial crack tip.

2.3. Mode I - Double Cantilever Beam test

The Double Cantilever Beam (DCB) test is performed to characterize the pure mode I fracture toughness at both the Delft University of Technology (TU Delft) and AMADE testing facilities of the University of Girona (UdG). The DCB tests at TU Delft follow the ASTM test standard [28] and loading blocks are bonded to load the specimens. In total, five tests are performed with an initial crack length of $a_0 = 40$ mm. The test configuration of the DCB test is shown in Fig. 2a and the experimental setup at UdG is shown in Fig. 2b. The DCB tests at UdG follow the ISO 15024 test standard [34] and the side-clamp beam [35] hinges are used to load the specimens, where the initial crack length is $a_0 = 48$ mm. As illustrated in Fig. 2a, the load-application point on the loading-blocks effectively reduces the crack length from the insert size of 60 mm to a_0. In additions to the five propagation test at TU Delft, several pre-cracks and three propagation tests are performed at UdG. The crack length during these additional propagation tests is closely monitored using the system as shown in Fig. 2b. A high resolution camera is used to monitor the crack length. Due to the limited field of view during close-up, a servo controlled system is used to follow the crack tip. The specimens are tested on a tensile testing machine, at a displacement rate of 1 mm/min. Rotation is measured by means of inclinometers. However, this data has not been used in the analysis and is not required for the proposed methodology. This also applies for all the other test configurations shown in this paper.

The Corrected Beam Theory (CBT) is used for the experimental data reduction method following the ISO 15024 test standard [34]. Following this method, the critical mode I energy rate G_{IC} is:

$$G_{IC} = \frac{3P\delta}{2b(a+\Delta)}\left(\frac{F}{N}\right) \tag{1}$$

where P and δ are the load and displacement, a is the total crack length during crack propagation and b is the specimen width. Furthermore, correction factors are used in the method, where F corrects for large displacement, N corrects for stiffening of the specimen by the loading blocks and Δ is a correction factor for crack tip rotation and deflection [34].

The experimental results are also compared to the analytical LEFM solution. For the Young's modulus E_{11} and E_{22}, the average of tension and compression from Table 1 is used. The analytical solution uses the equations for the compliance C and the G_{Ic} [36], which can be re-rewritten to calculate the force P and displacement δ:

$$P = \sqrt{\frac{G_{Ic}b^2h^3E_{11}}{12(a+\chi h)^2}} \tag{2}$$

$$\delta = \frac{8P(a+\chi h)^3}{bh^3E_{11}} \tag{3}$$

The crack tip correction χ is derived in Eq. (4) as

$$\chi = \sqrt{\frac{E_{11}}{11G_{13}}\left\{3 - 2\left(\frac{\Gamma}{1+\Gamma}\right)^2\right\}} \tag{4}$$

where Γ is the transverse modulus correction parameter defined as

$$\Gamma = 1.18\frac{\sqrt{E_{11}E_{22}}}{G_{13}} \tag{5}$$

In the elastic domain the load is used as input and Eq. (3) to calculate the corresponding displacement for a given initial crack length a_0. During propagation the crack length a is gradually increased, for a known G_{Ic}, to calculate both the force and the displacement.

2.4. Mode II - End-Notched Flexure test

The End-Notched Flexure (ENF) test [37], consists of a three point bending setup of a specimen that is cracked on one of its ends. Nowadays this test is adapted to characterize the mode II interlaminar fracture toughness. The test is standardized in ASTM D7905/D7905M [29] and is commonly used due to its simplicity, however the main drawback is that crack growth is often unstable. Fig. 3a shows the ENF test

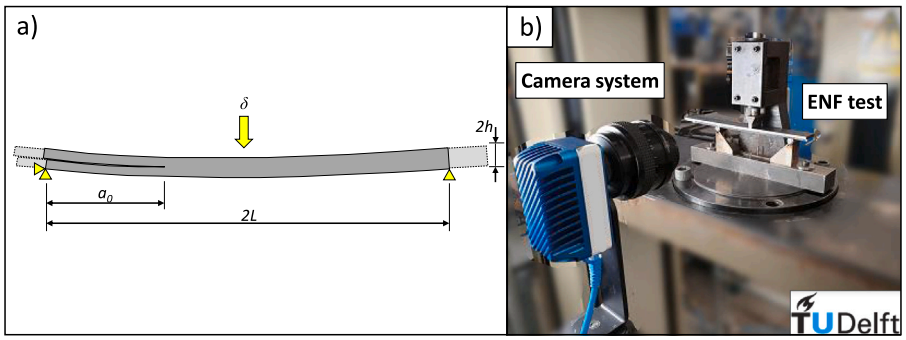

Fig. 3. ENF test setup at TU Delft lab: (a) ENF test configuration and geometrical parameters; (b) Test setup with camera system for crack monitoring.

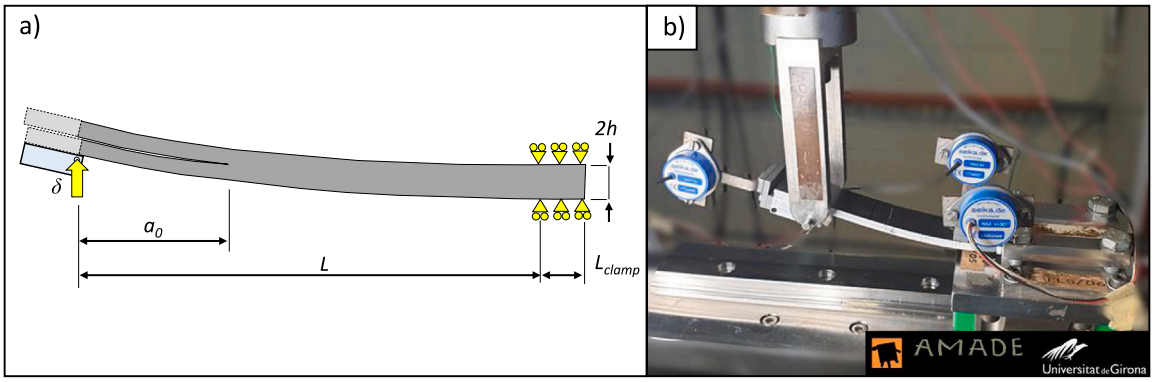

Fig. 4. CELS test setup at UdG AMADE lab: (a) CELS test configuration and geometrical parameters; (b) Test fixture and specimen.

configuration. The test setup at TU Delft including the camera to monitor the crack tip is shown in Fig. 3b. Tests are performed in order to determine the test configuration that would provide stable crack propagation in mode II. The initial tests were performed using a span of $2L = 100$ mm following the test standard. This made it difficult to achieve stable crack propagation due to the large fracture process zone. To solve this, the test configuration is adjusted to $2L = 130$ mm. The different results and settings to mitigate the large fracture process zone are further discussed in Section 3.2.

Most data reduction methods [29] depend on accurate measurements of the crack length during propagation. It is however difficult to measure this due to the development of a large fracture process zone ahead of the crack tip. The Compliance-Based Beam Method (CBBM) proposed by de Moura [19] can be used to avoid this. The measured initial compliance C_{0c} and initial crack length a_0 are used to obtain an apparent longitudinal modulus E_{1a}

$$E_{1a} = \frac{3a_0^3 + 2L^3}{8bh^3 C_{0c}} \tag{6}$$

Using the apparent modulus following [19] leads to

$$a_e = \left[\frac{C_c}{C_{0c}}a_0^3 + \left(\frac{C_c}{C_{0c}} - 1\right)\frac{2L^3}{3}\right]^{\frac{1}{3}} \tag{7}$$

where C_c is the measured compliance. Further combining the equations from [19] results in the mode II fracture toughness G_{IIC}

$$G_{IIC} = \frac{9P^2 C_{0c}}{2b(3a_0^3 + 2L^3)}\left[\frac{C_c}{C_{0C}}a_0^3 + \left(\frac{C_c}{C_{0C}} - 1\right)\frac{2L^3}{3}\right]^{\frac{2}{3}} \tag{8}$$

The experimental results are also compared to the analytical solution. In this case, the measured compliance is not available so a solution based on linear elastic fracture mechanics is followed. For this solution, the ENF load–displacement curve is divided into three parts. The load P is used as input for the first and third part and is gradually increased, while during crack propagation the crack length a is used as input to calculate both the load and the displacement. The crack length is corrected following [38], where χ is calculated from Eq. (4).

The load–displacement during the linear part is calculated by Eqs. (9) and (10) using $a = a_0$.

The second part during crack propagation if $a < L$:

$$P = \frac{\sqrt{G_{IIc}16b^2h^3E_{11}}}{9(a + 0.42\chi h)^2} \tag{9}$$

$$\delta = P\frac{3(a + 0.42\chi h)^3 + 2L^3}{8bh^3E_{11}} \tag{10}$$

and the third part where the crack has reached the load introduction if $a \geq L$:

$$\delta = \frac{P}{2E_{11}bh^3}\left(2L^3 - \frac{(\frac{16}{3}G_{IIc}E_{11}b^2h^3)^{\frac{3}{2}}}{4\sqrt{3}P^3}\right) \tag{11}$$

2.5. Mode II - Calibrated End Loaded Split

The ENF test showed some difficulties due to the large fracture process zone of the thermoplastic material, therefore the material is also characterized using the Calibrated End Loaded Split (CELS) test method so that the results can be compared. The CELS specimen with the corresponding geometrical parameters is shown in Fig. 4a and the test setup at the UdG lab is shown in Fig. 4b. The CELS test is performed in a test rig specifically designed according to the ISO 15114:2014 [30] test standard. A Loading block is bonded at the cracked end of the beam and an upward displacement is applied at the edge of the loading block. The other end of the beam is clamped, however this clamping is not fully constrained and allows for some sliding. The effect of the clamping system has to be calibrated so that an effective increase in beam length can be determined, as if the beam would be fully clamped. For this calibration procedure, the specimen is clamped and tested at several positions: 50, 60, 70, 80, 90 and 100 mm. The crack propagation test is performed at a clamp length of 100 mm with an initial crack length

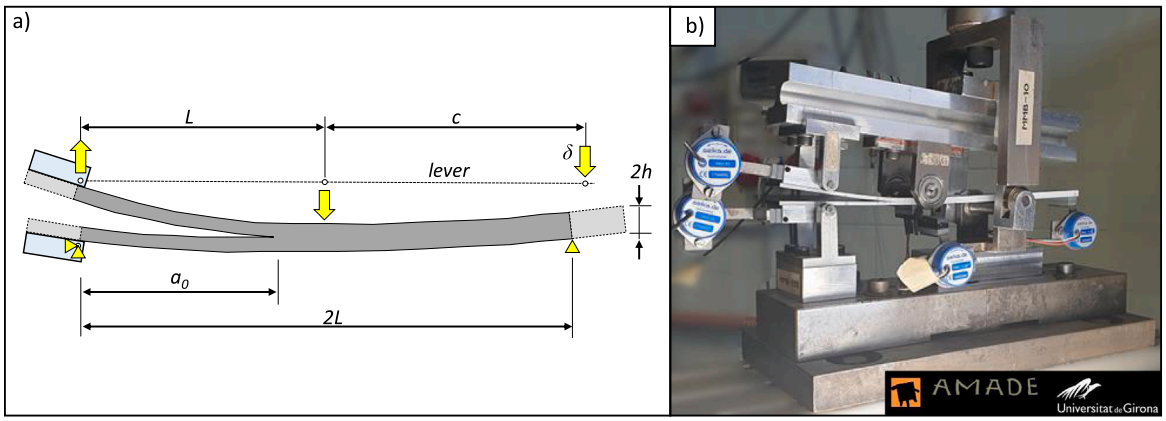

Fig. 5. Mixed-mode bending 50% setup at UdG AMADE lab: (a) MMB50 test configuration and geometrical parameters; (b) MMB test fixture and specimen.

of 56 mm. The crack length during propagation is measured using the same camera system as shown in Fig. 2b.

The experimental results are evaluated using the procedure according to the test method [30], where the compliance of the CELS specimen is given by:

$$C = \frac{\delta}{P} = \frac{3(a_e)^3 + (L + \Delta_{clamp})^3}{2bh^3 E_b} \tag{12}$$

where L, b and h are the span length, the width of the specimen and half of the specimen thickness, respectively. E_b is the apparent bending modulus and a_e is the effective calculated crack length. The Δ_{clamp} was introduced by Hashemi [36] to account for rotation and deflection at the clamp point. The parameters Δ_{clamp} and E_b are measured according to the compliance calibration described in the test standard [30]. The G_{IIC} fracture toughness is determined from

$$G_{IIC} = \frac{9P^2 a_e^2}{4b^2 h^3 E_b} \tag{13}$$

where the apparent crack length a_e is derived from Eq. (12) as

$$a_e = \left(\frac{1}{3}\{2bCh^3 E_b - (L + \Delta_{clamp})^3\}\right)^{\frac{1}{3}} \tag{14}$$

The experimental results are also compared to the analytical solution. The equations that are used to predict the CELS test are based on the CBT solution where the crack length is corrected ($a = a + 0.42\chi h$) [38] and the beam length L is increased by the clamp correction factor Δ_{clamp}. This can also be estimated by $2\chi h$ (assuming $\chi_0 = \chi$) [38], however it was found that this underestimates the clamp correction by approximately 5 mm, which highly influences the analytical prediction. The displacement in the elastic part can be derived by gradually increasing the load and by using a_0 in Eq. (16). The load and displacement during propagation are calculated by increasing the crack length for a known G_{IIc} following:

$$P = \sqrt{\frac{G_{IIc} 4b^2 h^3 E_{11}}{9(a + 0.42\chi h)^2}} \tag{15}$$

$$\delta = \frac{P(3(a + 0.42\chi h)^3 + (L + \Delta_{clamp})^3)}{2bh^3 E_{11}} \tag{16}$$

2.6. Mixed-mode bending 50%

The Mixed-Mode Bending (MMB) test [8] is used to characterize the fracture toughness under mixed-mode loading conditions. This test has been standardized in the ASTM D6671/D6671M-19 [31]. The MMB specimen with the corresponding geometrical parameters is shown in Fig. 5a and the test setup at the UdG AMADE lab is shown in 5b. The same camera system as shown in Fig. 2b is used to monitor the crack propagation. The mode mixity in this work is fixed to a ratio of 50% and only a single mode mixity is tested. The specimen has a pre-crack of length $a_0 = 40$ mm, which is pre-cracked for a few millimeter in mode I by means of the DCB test. Loading blocks are bonded to the specimen in order to clamp the bottom lever and load the upper lever as shown in Fig. 5. The span of the MMB50 test is set to $2L = 130$ mm to prevent interaction of the center load introduction point with the fracture process zone as observed during the mode II ENF test. The length of the lever arm, c, is set to 54.4 mm. The force due to the weight of the rig (P_g) is 9.129 N and the center of gravity (c_g) for the 50% mixed-mode test is at 12.95 mm. The modulus, width and thickness of the metal calibration specimens are $E_{cal} = 200$ GPa, $b_{cal} = 25.4$ mm and $t_{cal} = 6.21$ mm respectively. Following the test standard [31], this can then be used to calculate the system compliance and the bending stiffness of the laminate E_{1f}.

The mixed-mode fracture toughness is calculated by accounting for the weight of the test rig through Eqs. (17) and (18), but the influence is found to be neglectable (1%–2%) for the 50% mixed-mode test.

$$G_I = \frac{12[P(3c - L) + P_g(3c_g - L)]^2}{16b^2 h^3 L^2 E_{1f}}(a + \chi h)^2 \tag{17}$$

$$G_{II} = \frac{9[P(c + L) + P_g(c_g + L)]^2}{16b^2 h^3 L^2 E_{1f}}(a + 0.42\chi h)^2 \tag{18}$$

The experimental load–displacement curves are also compared to the analytical solution. The load–displacement curve for mixed-mode bending can be predicted following the LEFM equations from [39] that follow the ASTM standard [31]. The load is obtained as:

$$P = \sqrt{\frac{G_c}{\frac{4(3c-L)^2(a+\chi h)^2 + 3(c+L)^2(a+0.42\chi h)^2}{64bL^2 \frac{E_{11} bh^3}{12}}}} \tag{19}$$

The corresponding displacement is given as:

$$\delta = P\frac{4(3c - L)^2(a + \chi h)^3 + (c + L)^2[3(a + 0.42\chi h)^3 + 2L^3]}{96bL^2 \frac{E_{11} bh^3}{12}} \tag{20}$$

The elastic relation before crack propagation is obtained by replacing the crack length a with the initial crack length a_0 in the previous equations.

2.7. Methodology for derivation of cohesive laws

The traditional data reduction methods, as described in the previous sections, rely on accurate measurement or estimation of the crack length and do not provide sufficient information to account for fiber bridging or R-curve effects in the numerical analysis. These effects can be accounted for through the cohesive law. From literature it is known that different damage mechanisms can be represented by a different shape of the cohesive law. Three examples of typical shapes

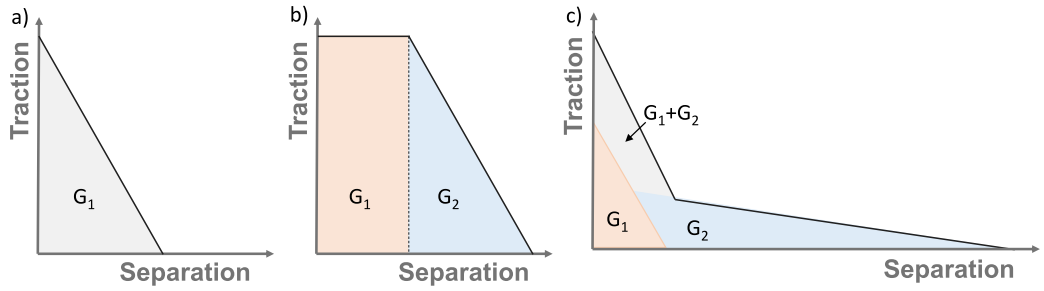

Fig. 6. Different shapes of cohesive laws used in numerical analysis to represent different damage mechanisms: (a) linear, (b) trapezoidal; (c) bilinear.

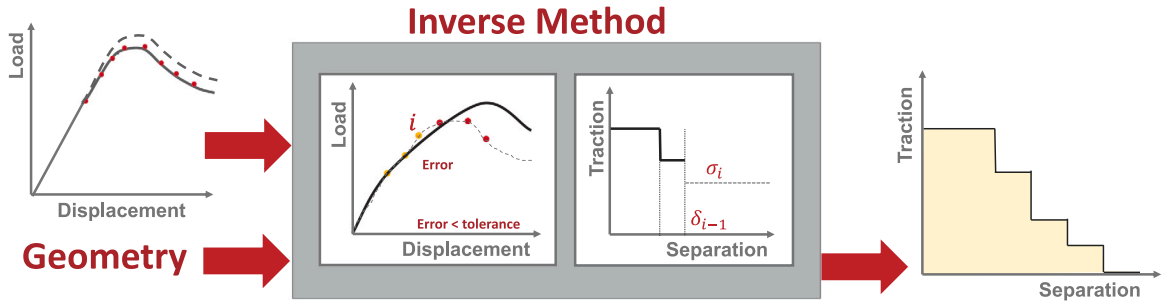

Fig. 7. Inverse methodology for derivation of cohesive laws, overview of methodology from [32,33].

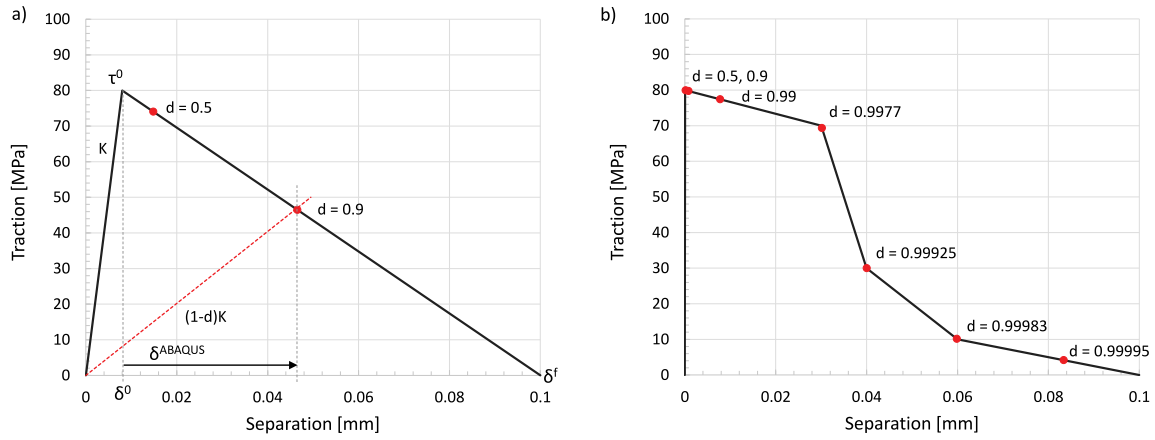

Fig. 8. Comparisons of two cohesive laws: (a) low penalty stiffness cohesive law with linear softening; (b) high penalty stiffness user-defined cohesive law.

for cohesive laws are shown in Fig. 6. Fig. 6a shows linear softening with is typically used by default when only the fracture toughness of the material is known. The trapezoidal shape as shown in Fig. 6b can be used to represent the influence of plasticity as demonstrated by Tvergaard and Hutchinson [40], where the total energy can be divided into multiple parts (G_1, G_2) to represent both plasticity and damage. Instead, different damage mechanisms may also be represented by superposition of linear cohesive laws to account for R-curve effects as shown in Fig. 6c based on the approach of Dávila et al. [23]. Dávila et al. used this bilinear shape to distinguish between fiber pull-out and breakage during translaminar failure [41], while a bilinear shape with a longer tail has been used to represent fiber bridging [24]. However, these simplified cohesive laws are generally not accurate enough to follow the full R-curve effect and corresponding nonlinearity observed in the load–displacement curve [24].

The proposed methodology, as shown in Fig. 1, can include the full R-curve effect and makes use of the inverse method presented by Abdel Monsef et al. [32,33] to determine the experimental J-curve and cohesive law. The inverse method minimizes the error between the experimental and the numerical load–displacement curves by adjusting the cohesive law parameters. Fig. 7 schematically shows the procedure to extract the cohesive law where the experimental load–displacement curve is the input and the output is an experimental J-curve and multilinear cohesive law "staircase type", also referred to as the experimental cohesive law in this paper. It should be noted that the method predicts only the shape of the cohesive law. This information may be used to reason that a specific damage mechanisms is responsible, study variation in cohesive laws between multiple tests, or gain insight in how the shape may change for different configurations or environmental conditions, as the methodology does not require visual tracking of the crack tip [42].

2.8. Procedure for user-defined tabular cohesive laws

The next step in the proposed methodology (Fig. 1b) is to process the experimental cohesive law for use in the numerical analysis, referred to as the numerical cohesive law. The cohesive law has to be defined by the initial elastic response of the cohesive element, the damage initiation criteria and the damage evolution. A typical traction–separation law with linear softening is shown in Fig. 8a. The

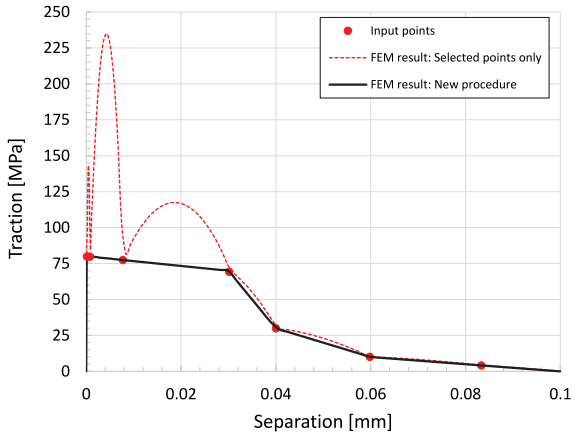

Fig. 9. Single element FEM result to verify tabular cohesive law.

initial elastic response of the element is related to the initial slope of the traction–separation curve, which can be related to the Young's modulus of the material when a finite thickness is used, for example for adhesives. For the analysis of delaminations, which are modeled as a zero-thickness interface, this property is referred to as the penalty stiffness (K in Fig. 8a). The damage initiation is defined as the peak traction for each loading mode by using a failure criterion, for example the max-stress criterion (MAXS). Damage evolution is provided in tabular format and requires the relation of the separation after damage initiation to the damage variable and the loading mode. The damage variable, d, is defined as the reduction of the effective traction due to damage as

$$d = 1 - \frac{\tau}{K \cdot \delta} \tag{21}$$

where τ is the traction at a material point, K is the initial elastic stiffness and δ is the total separation defined as $\delta = \delta^0 + \delta^{ABAQUS}$, as illustrated in Fig. 8a. δ^0 is the separation at onset of damage and δ^{ABAQUS} the input displacement for the tabular format in Abaqus. The loading mode, B, is defined as the ratio between pure mode I (defined as 0) and pure mode II (defined as 1), and has to be defined for each cohesive law that results from the mixed-mode tests.

It is however difficult to achieve an accurate solution for detailed cohesive laws when using a high penalty stiffness or when a sudden change in the shape of the cohesive law are introduced. When a low penalty stiffness is used, the damage variable gradually increases until full separation is achieved as shown in Fig. 8a. However, when using a high-penalty stiffness, as shown in Fig. 8b, there is rapid increase in the damage variable for small separation until the element is nearly fully damaged ($d = 0.99$). This is followed by a rapid increase in displacement until the element is fully damaged, which means high accuracy is required in both damage and displacement. If sudden changes or complex shapes are introduced in the cohesive law, it becomes even more difficult to manually define accurate input data.

When using a high penalty stiffness, for example $K = 10^6$ N/mm^3, which is typically used for simulation of delaminations, another difficulty arises. It appears that Abaqus uses a higher-order interpolation function for cohesive laws in tabular format, which may cause spurious oscillations if insufficient data points are defined. A simulation of a single cohesive element that highlights this issue is shown in Fig. 9 on the same cohesive law as presented in Fig. 8b. When using only the selected points in the tabular cohesive law, defined as "Input points" in Fig. 9, spurious behavior is observed. In order to solve this, a procedure is developed that will guarantee an accurate description of the tabular cohesive law.

The flow diagram of this procedure is shown in Fig. 10. The input for the methodology is the shape of the cohesive law which should contain each line segment. The experimental cohesive law first needs to be simplified or cleaned to ensure the J-curve and damage variable monotonically increase. This means that typically only small adjustments are required to directly use the shape of the experimental cohesive law. However, it was found that a more smooth shape helps convergence as it reduces sudden changes in stiffness. During this calibration process it is important to ensure a close correlation with the experimental J-curve, to guarantee that the same amount of energy is dissipated at each segment of opening displacement. In order to adjust the desired accuracy of the tabular procedure, a constraint to the maximum increase

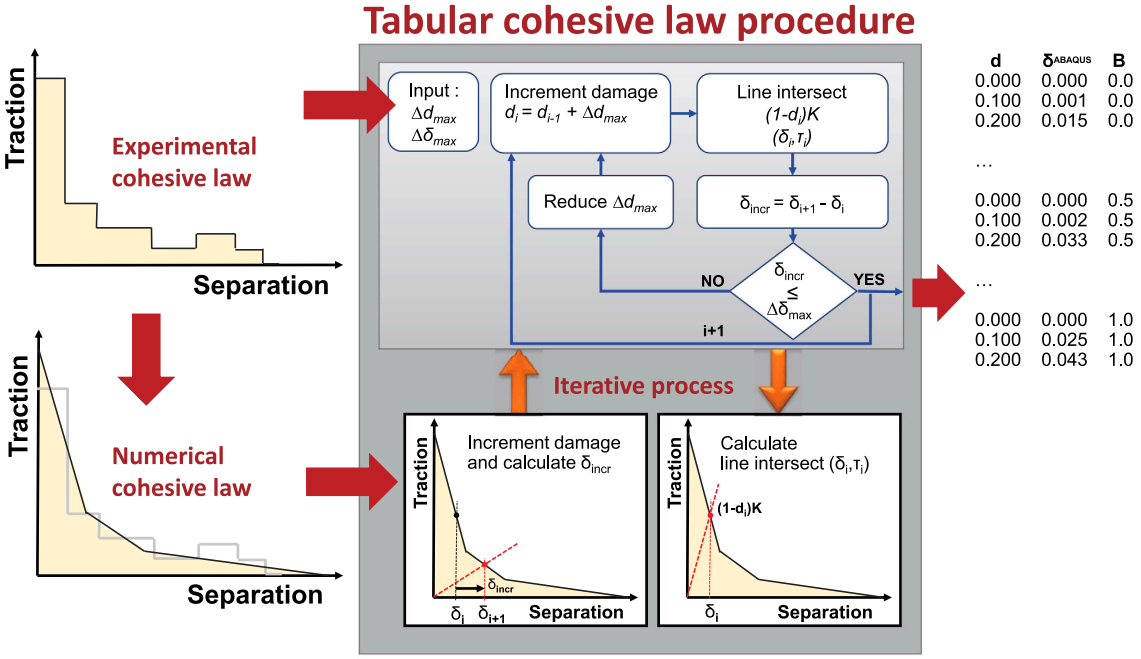

Fig. 10. Procedure for user-defined tabular cohesive law.

in damage variable $\triangle\ d_{max}$ and displacement $\triangle\ \delta_{max}$ is introduced. The damage variable is gradually increased from 0 to 1 by using the maximum damage variable as a step size, and will thus influence the table size. The resulting penalty stiffness is then calculated from Eq. (21) and is used to calculate the line-segment intersection of the cohesive law. The displacement at onset of damage ($\delta^0 = \tau^0/K$) is then subtracted for the displacement at the increment (δ_i) of the line-segment intersection in order to calculate the delta displacement. This increase in displacement (δ_{incr}) is checked against the constraint. If this criteria is not met, the increase in damage variable is reduced and the procedure is repeated until the criteria is met. This value is then saved in tabular format and the damage is further increased. This is repeated for each cohesive law and loading mode. The FEM result to verify the procedure on the high-penalty stiffness cohesive law is shown in Fig. 9 by comparing the input points to the resulting cohesive law. This demonstrates that the cohesive behavior can be accurately simulated using the tabular approach.

3. Experimental results

The experimental results for each test are presented and evaluated using the two data reduction approaches. The load–displacement curves are compared to the analytical solution for each test and the R-curves are presented. Furthermore, the experimental J-curves and cohesive laws are processed for the numerical analysis and compared against the experimental curves.

3.1. Mode I - Double Cantilever Beam

All the mode I experimental results including pre-cracking are shown in Fig. 11. As can be observed in the figure, DCB with different initial crack lengths are performed and also several pre-crack tests are performed. One typical test is selected for data reduction in the next section. The relation of this specific test to the other tests is then further investigated and discussed.

The load–displacement curve of the selected test is compared to the analytical solution in Fig. 12a and the corresponding R-curve is shown in Fig. 12b. The load–displacement curve consists of a pre-crack and a propagation part, which were tested separately and they are compared to the analytical solution using $a_0 = 48$ mm and $G_{Ic} = 1.12$ kJ/m^2. The first marker on the curve indicates the 'NL point' (first deviation from linear portion of curve) and all other points represent visible observations of crack growth and are indicated as 'PROP'. The same points are plotted in the R-curve with their corresponding calculated fracture toughness from the data reduction method. The initiation fracture toughness is approximately 0.7 kJ/m^2 and the propagation fracture toughness 1.12 kJ/m^2. The resulting experimental J-curve and cohesive law that are determined using the inverse method are shown in Fig. 13a and b, respectively. For reference, the processed numerical J-curve and cohesive law which will be used as input for the numerical analysis are also given.

When taking a closer look at Fig. 13a it is found that the experimental results show a plateau in the J-curve and an increase in fracture toughness at a crack opening larger than 0.5 mm. In the cohesive law of Fig. 13b, this effect is visible as the long tail, while most of the energy dissipates at the start of the cohesive law. This effect can also be observed experimentally as shown in Fig. 14a. The experiment shows large scale fiber bridging and many broken fibers on the fracture surface. The fracture surface is also investigated by means of Scanning Electron Microscopy (SEM) at UdG. This is shown in Fig. 14b with a magnification of 300x, and shows pull-out of large fiber bundles on the fracture surface. A close-up using 1000x magnification in Fig. 14c of a fiber bundle highlights extensive polymer drawing out in the plane normal to the fiber direction and a large presence of polymer material on the fibers.

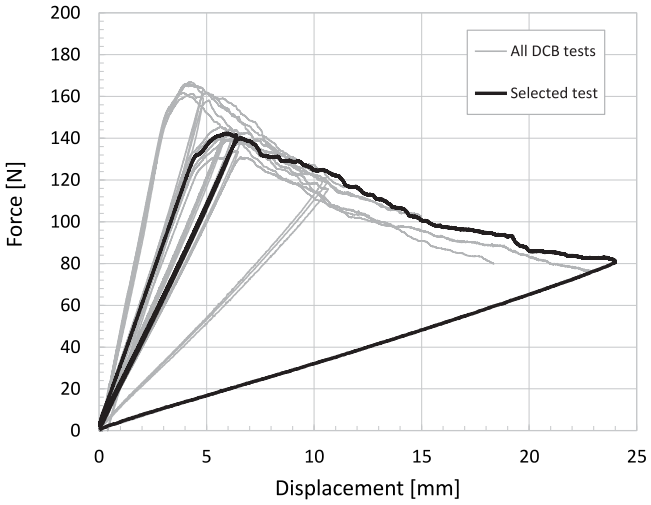

Fig. 11. DCB test results, selected test for initial evaluation highlighted.

The influence of fiber bridging is investigated further by comparing several DCB tests. This comparison is shown in Fig. 15a and all tests show a consistent initiation fracture toughness of approximately 0.7 kJ/m^2, independent of initial crack length. However, the second test (Fig. 15a, DCB 2) achieves a propagation fracture toughness of approximately 0.95 kJ/m^2, which may suggest a smaller influence of fiber bridging.

This is confirmed by comparing the experimental J-curves and cohesive laws. This comparison is shown in Fig. 15b, where the scale of the experimental cohesive law is adjusted to zoom in on the tail. It is shown that, as the opening displacement increases, the propagation fracture toughness of the first test increases to approximately 1.12 kJ/m^2 (I). This increase in energy can also be observed in the experimental cohesive law, which makes it apparent that energy is being dissipated due to fiber bridging (II). However, this is not the case for the second test, which reaches a plateau in the J-curve and no dissipation of fracture energy is observed in the tail of the cohesive law (III). The plateau in the J-curve of Fig. 15b suggests that scatter in the propagation fracture toughness may be mostly influenced by the amount of fiber bridging, and that fiber bridging may not play an important role for small cracks (<0.5 mm opening displacement). The proposed methodology could be used to further investigate scatter in the interlaminar properties and establish a lower, mean and upper-bound J-curve. The J-curve can then be used to treat variation in different parts of the cohesive law separately. This insight may be used to support studies on uncertainty quantification related to variability of the interlaminar behavior. It should also be noted that discarding the pre-crack part of the load–displacement curve and using only the propagation value in the numerical analysis would be unconservative for small cracks.

3.2. Mode II - End-Notched Flexure

The interlaminar properties for mode II are characterized by means of the End-Notched Flexure (ENF) test. The result of three ENF tests are shown in Fig. 16 and are compared against the analytical solution. The first (1) two tests are performed following the test standard with a span of 100 mm and initial crack length of $a_0 = 40$ mm. Very little stable crack propagation is measured because of the large fracture process zone that interacts with the load introduction point. Significant shear deformation is observed over a large area. However, the exact size is difficult to determine which support the choice of using an effective crack length during the data reduction instead. Interaction with the

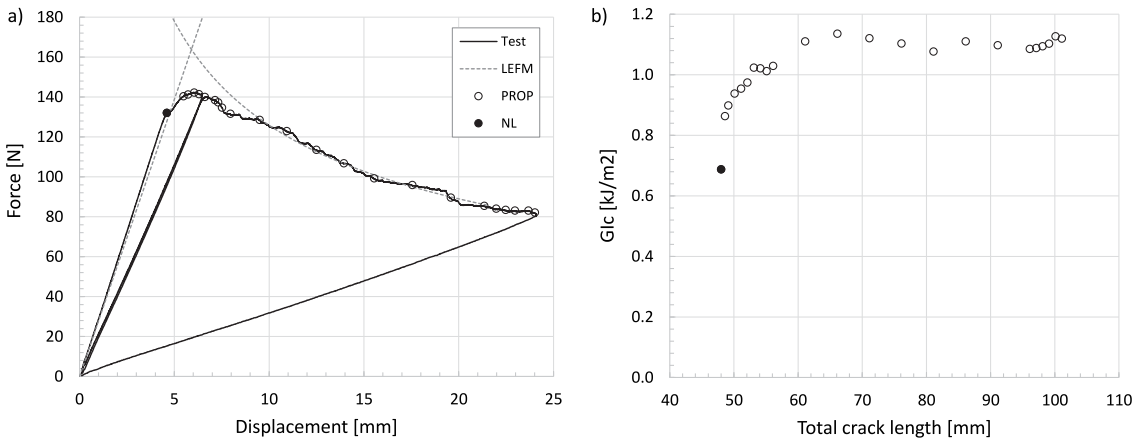

Fig. 12. DCB test result: (a) Load–displacement vs. analytical solution (LEFM), nonlinear (NL) and crack propagation points (PROP); (b) R-curve with propagation points.

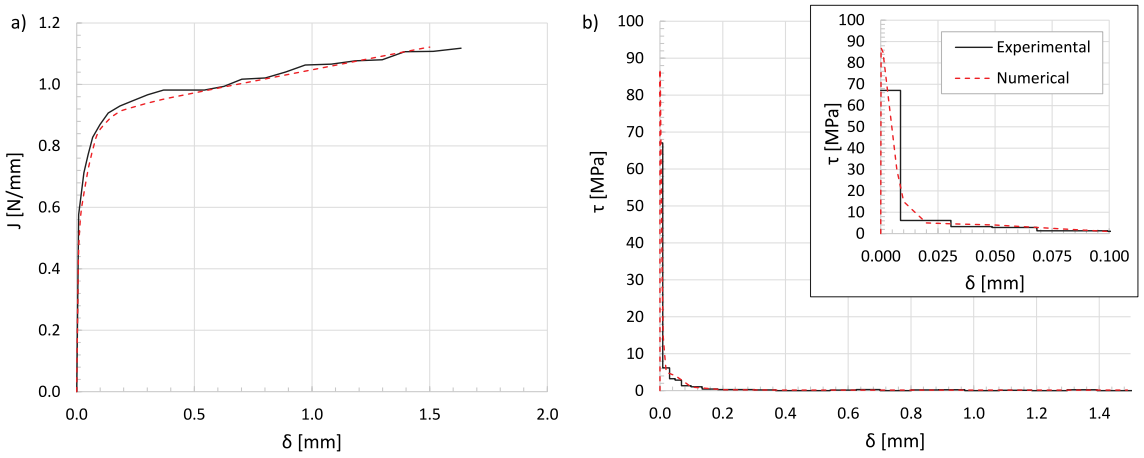

Fig. 13. DCB data reduction, experimental and numerical curves: (a) J-curve; (b) Cohesive law.

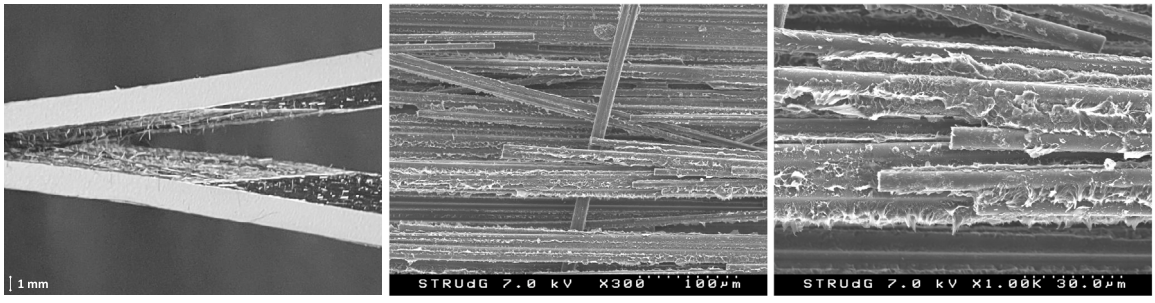

(a) (b) (c)

Fig. 14. Experimental evidence of fiber bridging: (a) Fiber bridging and broken fibers during DCB test; (b) SEM fracture surface showing pull-out of large fiber bundles; (c) SEM close-up on fiber bundle.

load introduction point is also well predicted by the third part of the analytical solution of the ENF test in Eq. (11). In order to mitigate this issue, the test setup is adjusted (2) to $a_0 = 45$ mm and span of $2L = 130$ mm. The specimens are pre-cracked in mode I prior to testing. For both configurations a good correlation with the analytical solution is found.

This highlights that it is difficult to achieve stable crack propagation with the ENF tests for materials that develop a large fracture process zone such as thermoplastic composites. In literature, a value of $a/L > 0.7$ is typically suggested [4] to achieve stable crack propagation. While testing at a small a/L ratio results in unstable crack growth [43]. The downside to a too large a/L is that it reduces the available room to develop the fracture process zone before achieving stable crack propagation ($L - a$). During the first test in Fig. 16, the configuration was $a/L = 0.8$ and $L - a = 10$ mm which is found to be insufficient. The configuration of the second test was $a/L = 0.7$ and $L - a = 20$ mm and worked well, thus achieving a full development of the fracture process zone. The lower bound related to unstable crack propagation is not investigated, but it is likely that configurations in the range of $0.65 < a/L < 0.75$ would provide good results for this material system.

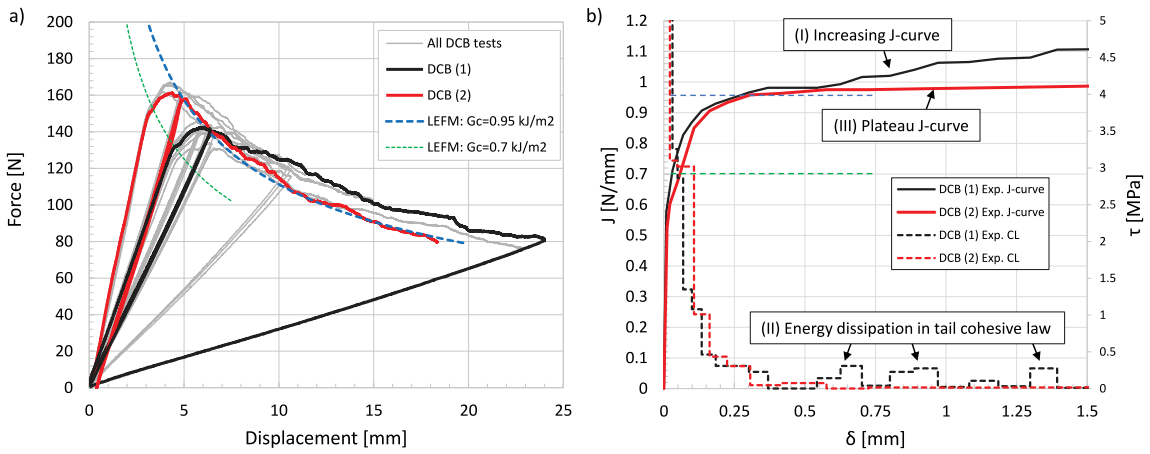

Fig. 15. Fiber bridging influence on Mode I: (a) DCB tests with two selected results and comparison against analytical solution of $Gc = 0.7$ kJ/m^2 and 0.95 kJ/m^2; (b) Corresponding J-curve and cohesive law for both tests with identification of initiation and fiber bridging Gc.

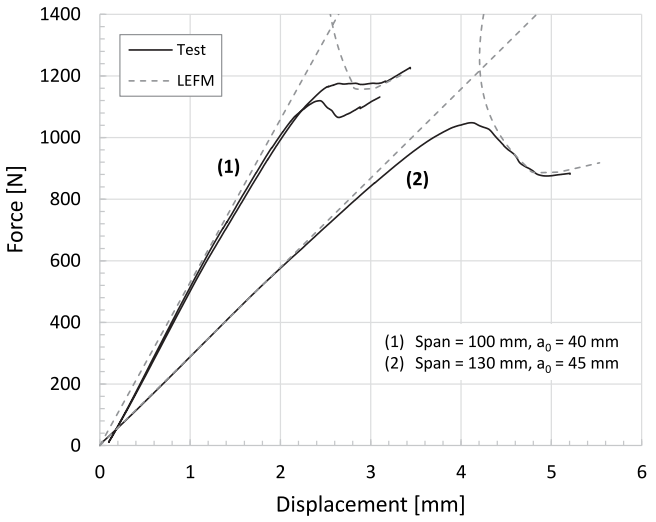

Fig. 16. ENF experimental results versus analytical solution.

The load–displacement of the ENF test is compared in Fig. 17a against the analytical solution ($a_0 = 45$ mm and $span = 130$ mm) for $G_{IIc} = 2.35$ kJ/m^2. The initiation fracture toughness appears to be rather low and similar to the mode I initiation value. This is shown in the R-curve of Fig. 17b for both the DBT [19] and CBBM data reduction method from Eq. (8). The calculated crack length from the CBBM method results in a different crack length compared to what is visually observed. However, the propagation fracture toughness is nearly identical, with the benefit that no visual observation of crack propagation is required when using the effective crack length method. The resulting experimental J-curve and cohesive law are shown in Fig. 18a and b, respectively. For reference, the processed numerical J-curve and cohesive law which are then used as input for the numerical analysis are also given.

3.3. Mode II - Calibrated End Loaded Split

The interlaminar properties for mode II are also characterized by means of the Calibrated End Loaded Split (CELS) test. Experimental results for the three CELS tests are shown in Fig. 20a. The tests are performed at a clamp length of 100 mm. The load–displacement of one CELS test is highlighted in Fig. 20a and compared against the analytical LEFM solution. From the calibration, a clamp correction of 13.64 mm and a bending modulus of 134 339 MPa is calculated.

The compliance, C, of the individual tests at different clamp lengths is plotted in Fig. 19 using $C^{1/3}$ to calculate Δ_{clamp} at the intercept of the regression line.

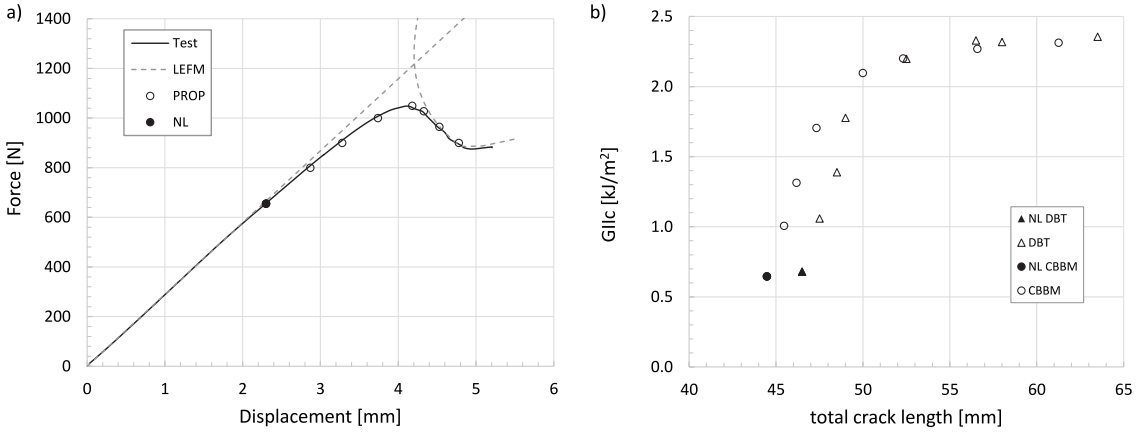

Fig. 17. ENF test result: (a) Load–displacement vs analytical (LEFM), nonlinear (NL) and crack propagation points (PROP); (b) R-curve with propagation points for both the DBT and CBBM data reduction method.

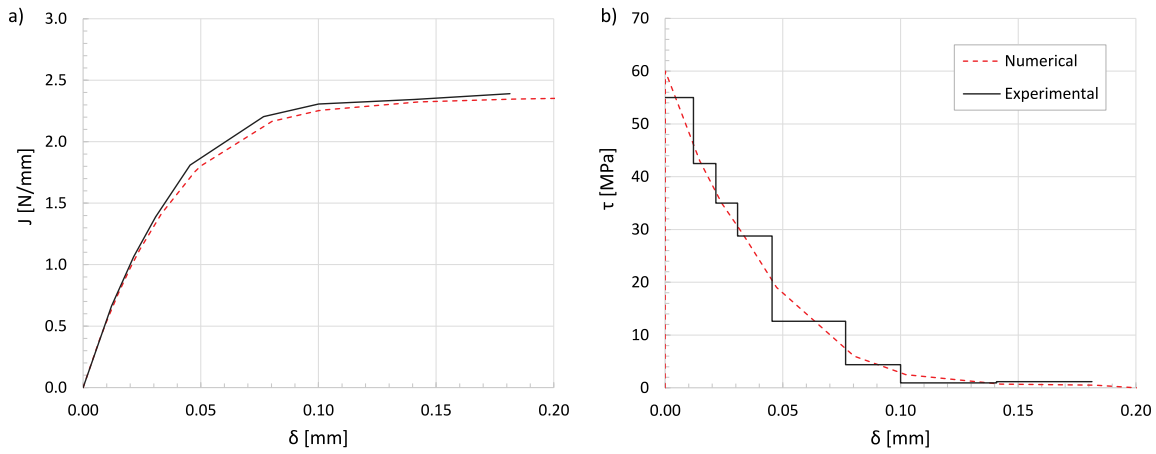

Fig. 18. ENF data reduction, experimental and numerical curves: (a) J-curve; (b) Cohesive law.

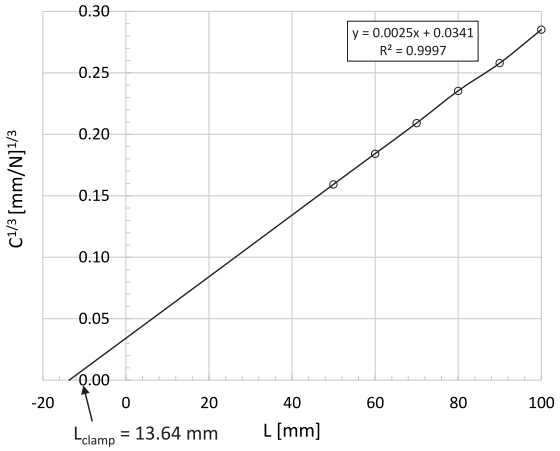

Fig. 19. CELS test calibration results and calculated clamp correction L_{clamp}.

The R-curve using both the visual and effective crack length is shown in Fig. 20b. The effective crack length method results in a significantly higher crack length and fracture toughness compared to using the visual crack length in Eq. (13). The propagation fracture toughness of the effective crack data reduction method shows a good correlation with the LEFM solution from Eqs. (15) and (16), and accounts for both the crack tip and clamp correction.

The resulting experimental J-curve and cohesive law are shown in Fig. 21a and b, respectively. The calculated fracture toughness based on the effective crack length shows a good match with LEFM (G_{IIc} = 2.35 kJ/m^2). The experimental J-curve and cohesive law are determined using a total length including clamp correction of $L+\Delta_{clamp}$ = 113.6 mm in the inverse method. It is observed that at an opening displacement of 0.15 mm the J-curve reaches a plateau around J = 2.35 N/mm and the cohesive law approaches zero. After some more crack opening the energy further increases. This effect is also visible on the load–displacement and R-curve and is consistent with the data reduction method based on the effective crack length in terms of fracture energy. For reference, the processed numerical J-curve and cohesive law from the ENF test (Fig. 18) are also given and it shows that they are nearly identical. This demonstrates that the J-curve is independent of the test configuration and consistent behavior between the two tests is found, even though the tests are performed at different test facilities.

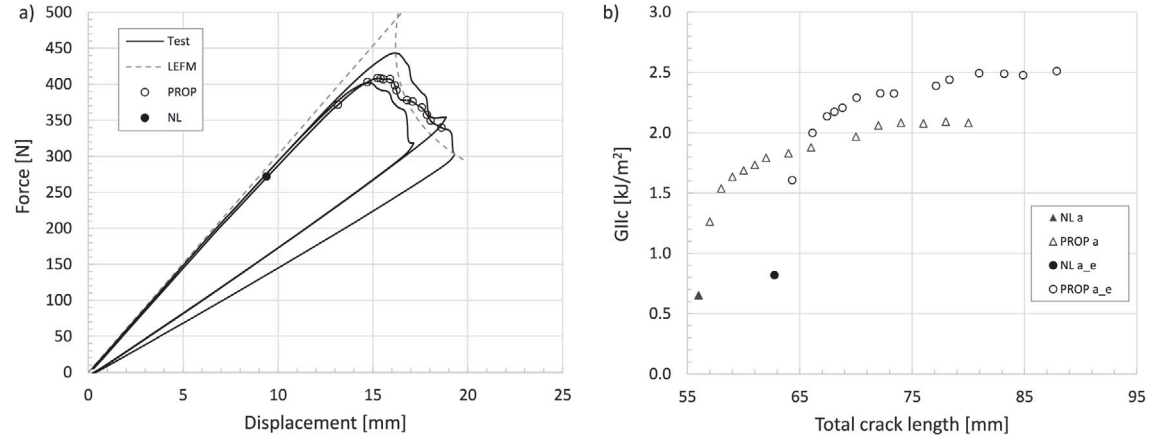

Fig. 20. CELS test result: (a) Load–displacement vs analytical (LEFM), nonlinear (NL) crack propagation points (PROP); (b) R-curve with propagation points using visual (PROP a) and effective crack length (PROP a_e) with clamp correction.

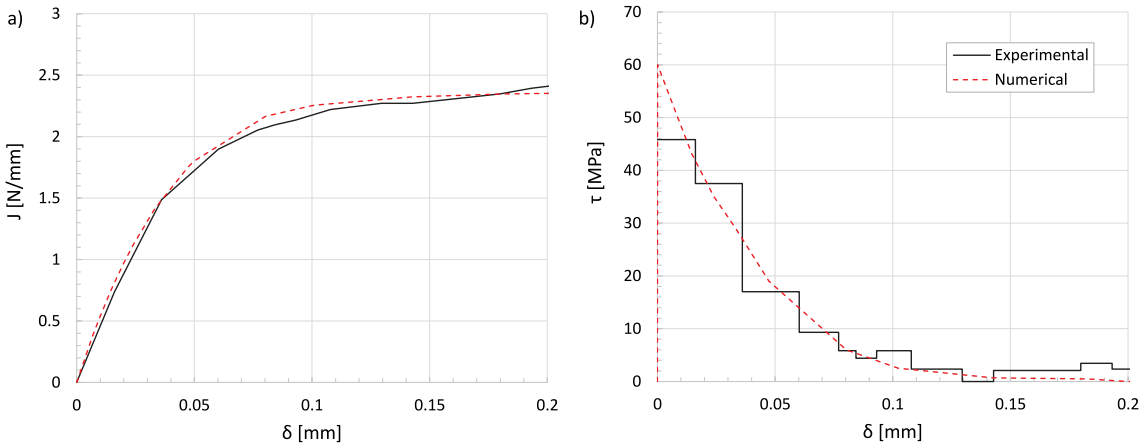

Fig. 21. CELS data reduction, experimental and numerical curves: (a) J-curve; (b) Cohesive law.

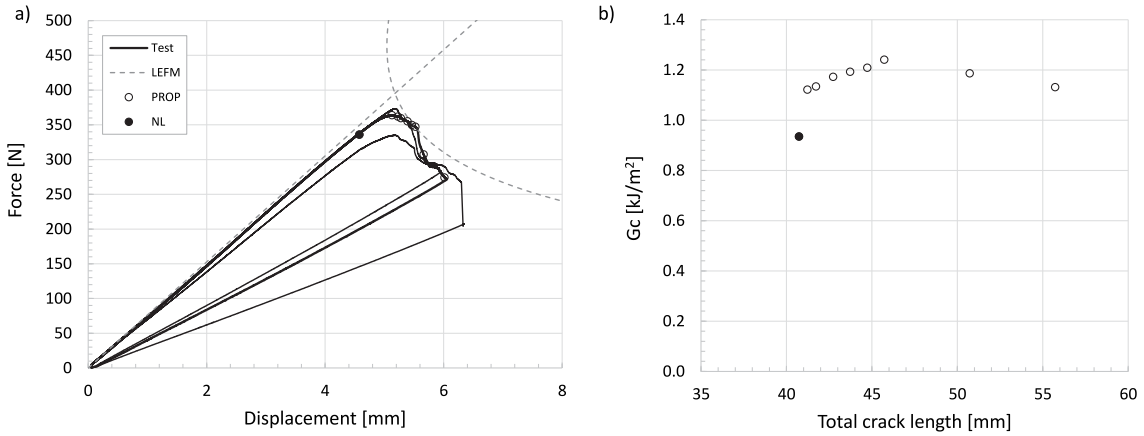

Fig. 22. Mixed-mode bending 50% test result: (a) Load–displacement vs analytical (LEFM), nonlinear (NL) crack propagation points (PROP); (b) R-curve with propagation points.

3.4. Mixed-mode bending 50%

The interlaminar properties for mixed-mode behavior are characterized by means of the Mixed-Mode Bending (MMB) test. The load–displacement curves of three MMB tests at 50% mode I–II are shown in Fig. 22a. The load–displacement curve of one of the MMB50 tests is compared against the analytical LEFM solution using a initial crack length of $a_0 = 40$ mm, $G_{Ic} = 1.12$ kJ/m^2, $G_{IIc} = 2.35$ kJ/m^2 and a BK-coefficient [44] of 2.9, which results in a mixed-mode fracture toughness of 1.27 kJ/m^2. This comparison is shown in Fig. 22a, which matches well with the R-curve presented in Fig. 22b. It is observed in the R-curve that after some crack propagation, the calculated fracture toughness reduces, which may be caused by interaction of the fracture process zone with the load-introduction or changes in mode-mixity during crack propagation.

3.5. Fractographic investigation

A fractographic investigation using SEM is performed to provide insight into the interlaminar damage mechanisms during Mode I, Mixed Mode I/II at 50:50 and Mode II loading conditions. The SEM micrographs at different magnifications for each loading mode are presented in Fig. 23. Experimental evidence of fiber bridging by means of SEM micrographs is already presented in Fig. 14. The Mode I fracture surface of a matrix rich location is shown in Fig. 23a and b. Extensive polymer drawing out in the plane normal to the fiber direction is observed. At several locations this occurred in circular patterns and signs of plastic deformation are present. The circular pattern in the fracture surface, and signs of patterns in the fiber beds, may suggest a relation of the matrix-dominated failure mode with the crystallization kinematics of the thermoplastic polymer matrix as they appear to be similar is size [45]. During loading in Mixed Mode I/II at 50:50 the presence of plastic deformation is even more pronounced and occurs at an angle to the fiber direction as shown in Fig. 23c and d. The change in angle is further confirmed by the CELS Mode II fracture surface as shown in Fig. 23e and f, which features polymer drawing out and extensive plastic deformation in the plane of the delamination. The SEM micrographs confirm the absence of fiber bridging in Mixed Mode I/II at 50:50 and Mode II loading conditions. These observations are in line with Carlsson et al. who compared the fracture surface in mode I and II of epoxy matrix and PEEK thermoplastic matrix composites, and found very brittle behavior showing bare fibers and a small degree of polymer deformation for the epoxy matrix composites in mode I, and extensive hackling in mode II. The presence of plastic deformation in both his and the present work confirms that energy dissipation due to plastic deformation plays are important role in the interlaminar fracture behavior of thermoplastic matrix composites.

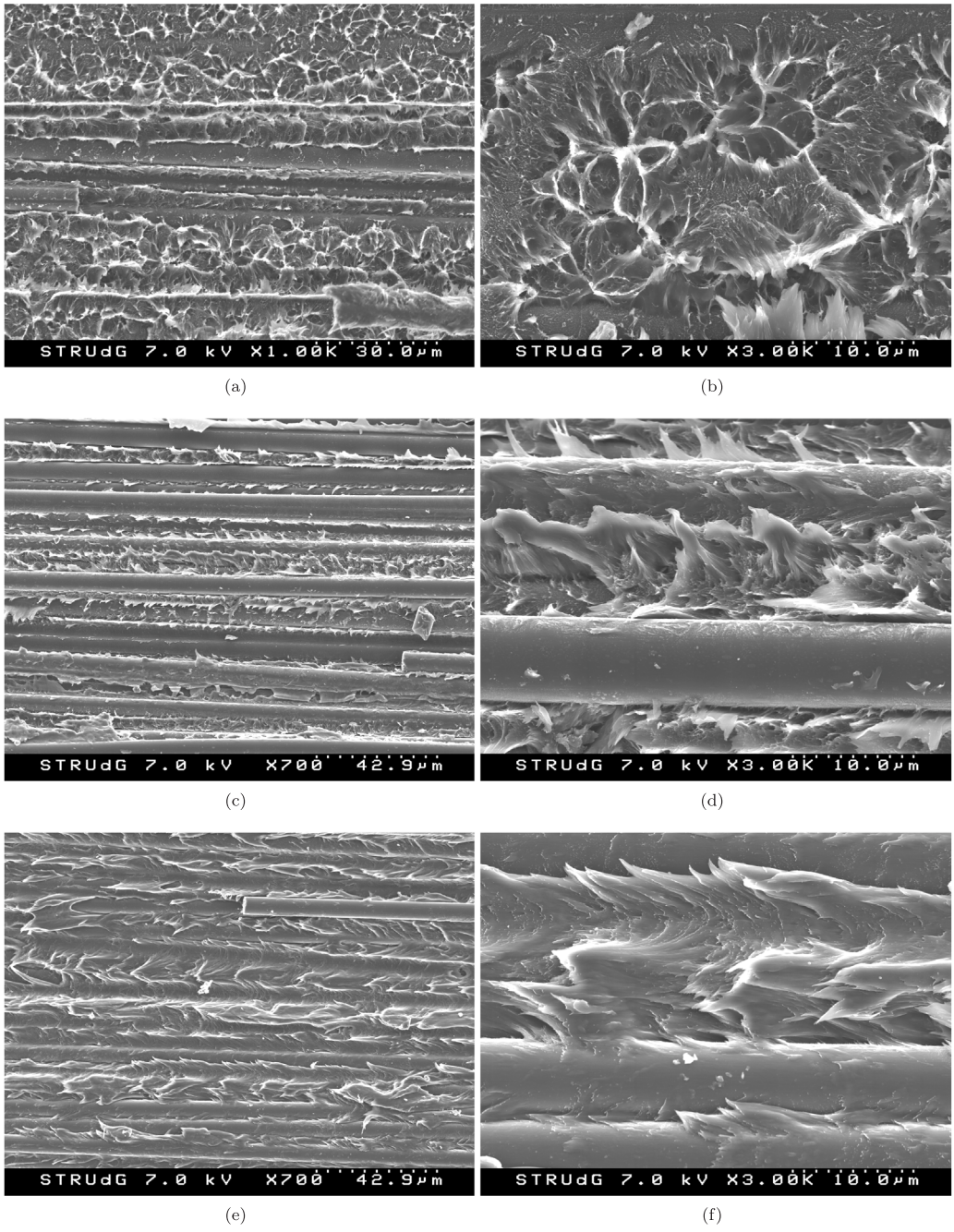

Fig. 23. SEM micrographs of fracture surface at different magnifications: (a) Mode I 1000x; (b) Mode I 3000x; (c) Mixed Mode I/II at 50:50 700x; (d) Mixed Mode I/II at 50:50 3000x; (e) CELS Mode II 700x; (f) CELS Mode II 3000x.

4. Analysis and discussion

Numerical analyses of the Double Cantilever Beam (DCB), End-Notched Flexure (ENF), Calibrated End Loaded Split (CELS) and Mixed-Mode Bending 50% (MMB50) tests have been simulated by using the commercially available finite element software ABAQUS/Standard. The result of both data reduction approaches as defined in Fig. 1 are simulated in order to verify the derived interlaminar behavior and analysis methodology. The specimens are modeled by using two-dimensional plane strain elements (CPE4I) for the composite laminate and COH2D4 cohesive elements for the interface. A fine mesh of 0.1 mm is used to ensure that sufficient elements are within the fracture process zone [46]. The rolling conditions of the CELS test are not modeled, instead the beam length is increased by the clamp correction length and fixed.

Table 2
Summary of geometric parameters used in the numerical analysis.

Test	W [mm]	$2h$ [mm]	a_0 [mm]	L [mm]	L_{clamp} [mm]	c [mm]
DCB	25	4.2	40/48	100	–	–
ENF	25	4.2	40	65	–	–
CELS	25	4.2	56	100	13.64	–
MMB50	25	4.2	40	65	–	54.4

The values for the relevant geometric parameters that are used in the numerical analysis are summarized in Table 2 and the geometry follows the configurations as specified in Section 2.

The elastic material properties that are used in the analysis are specified in Table 1. For the Young's modulus E_{11} and E_{22}, the average

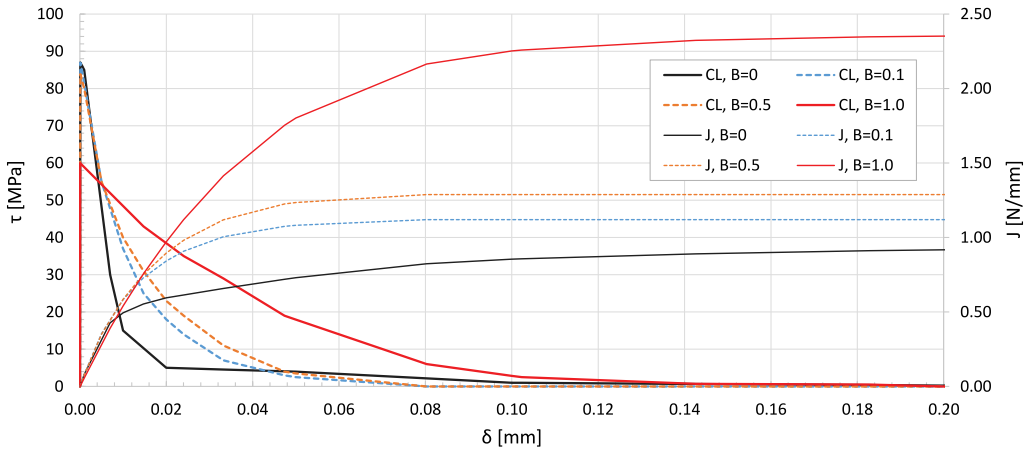

Fig. 24. Summary of numerical cohesive laws and corresponding J-curves.

of tension and compression is used. The initiation strength values of the numerical cohesive laws are based on the prediction from the experimental cohesive laws and are aligned to the strength values reported in [15]. Therefore, the mode I initiation strength is set equal to the matrix tensile strength Y_T of 87 MPa. However, the mode II initiation strength is not set equal to the matrix 5% offset shear strength S_L. Damage initiation in mode II occurs at a much smaller shear strain [47], therefore the mode II initiation strength value is set to the 0.5% offset shear strength of approximately 60 MPa. The value is estimated from the nonlinear parameters and equations in [15]. For the penalty stiffness of the interface, a value of $K = 10^6$ N/mm^3 is used. Considering the amount of plastic deformation on the fracture surface in Fig. 23, and predicted initiation strength by the inverse method in the range of 45–60 MPa, it becomes apparent that a large portion of the fracture energy at the start of the cohesive law is likely due to plastic deformation. Depending on the choice of shear initiation strength, this would results in either an exponential or trapezoidal shape of the cohesive law. In the current work, an exponential shape is assumed. It is also expected that constraining effects of different fiber orientations on plasticity may need to be considered. However, this is not included in the present study. In Section 3.1 it is shown that fiber bridging has a significant influence on the mode I fracture toughness. It is concluded that the propagation fracture toughness without the influence of fiber bridging is approximately 0.95 kJ/m^2 and no clear signs of fiber bridging are observed during evaluation of the mode II and mixed-mode 50% test. This means that the BK-coefficient [44] for mixed-mode behavior could be calculated with or without the influence of fiber bridging for simulations that do not take into account R-curve effects. The BK-coefficient with the influence of fiber bridging is 2.9 and without is 2.1. The cohesive laws derived for Mode I and II as defined in Section 3 are implemented into a single material card in tabular format, considering the mixed-mode behavior. It is assumed that the shape of the mixed-mode 50% follows an exponential form, similar to mode II, while respecting the mixed-mode fracture energy and initiation stress according to the BK-criterion including fiber bridging. A summary of the numerical cohesive laws and corresponding J-curves are given in Fig. 24.

The simulation results of using both tabular and linear cohesive laws are compared against the experimental load–displacement and analytical solutions in Fig. 25 for all the different test configurations. The results for the DCB simulation are shown in Fig. 25a and the simulation using the tabular cohesive law matches the experimental load–displacement curve and the R-curve effect with high accuracy. When using the traditional data reduction approach and only the propagation fracture toughness in the numerical analysis, similar results as the analytical LEFM solution are achieved. This means that the numerical results will be inaccurate and unconservative for cracks smaller than 15 mm as also indicated by the R-curve in Fig. 12.

Simulating the mixed-mode bending 50% test using linear softening and low initiation strength in mode II, results in early propagation and inaccurate predictions, as explained in more detail in [20] and is solved by setting the shear initiation strength to the 5% matrix shear strength $S_L = 90$ MPa. This results in the correct propagation behavior as shown in Fig. 25b, but no R-curve effect is observed. Initially, the mixed-mode bending 50% test also showed some issues for the tabular approach. A large mismatch during propagation as indicated by the red dotted line in Fig. 25b is observed. It is found that this may be caused by the large difference in shape of the mode I and II cohesive laws due to fiber bridging, which may result in incorrect interpolation for the modes that are not included in the tabular format. Fiber bridging was not observed during the MMB50 test, however the exact mode-mixity at which this effect is not present anymore is not determined experimentally, but it is assumed to be close to mode I. It is there decided to insert another cohesive law at a mixed-mode of 10% to cut the fiber bridging contribution from the total fracture toughness. It was found that the J-curve of the 10% and 50% cohesive laws need to reach their propagation values according to BK [44] at a much shorter opening displacement compared to mode I. From this it can be concluded that the BK interpolation is valid for the total energy, but not for the individual parts of the J-curve as shown in Fig. 24. The difference between including the additional cohesive law at 10% mode mixity (B = 0.1) is further investigated using the MMB50 test. It is found that a significant change in the size of the fracture process zone is observed and also a large difference in mode-mixity as damage progresses. This is shown in Fig. 26 which shows the ABAQUS field output *mode mix at damage evolution (MMIXDME)* for the two different configurations. Therefore, it would be beneficial to perform additional experimental tests at different mode mixity, but it also demonstrates that the new tabular approach can be used to easily estimate the intermediate shapes of the cohesive law and it is not constrained to a fixed mixed-mode interaction for the whole J-curve.

It is also shown that both the ENF and CELS test can be predicted using the same cohesive law by comparing the numerical analysis with the experimental results in Fig. 25c and d, thus showing that the cohesive law is independent of the test configuration. Using the low initiation strength already predicts part of the initial nonlinearity in the ENF load–displacement curve as shown in Fig. 25c, and using the tabular cohesive law further improves this. For the CELS test, as shown in 25d, the numerical analyses predicts the average of the experimental load–displacement curves with an improvement in the initiation when using the tabular approach. Summarizing, it is concluded that by using the proposed methodology the experimental load–displacement curves can be accurately predicted for all four tests, while using only a single material card as input.

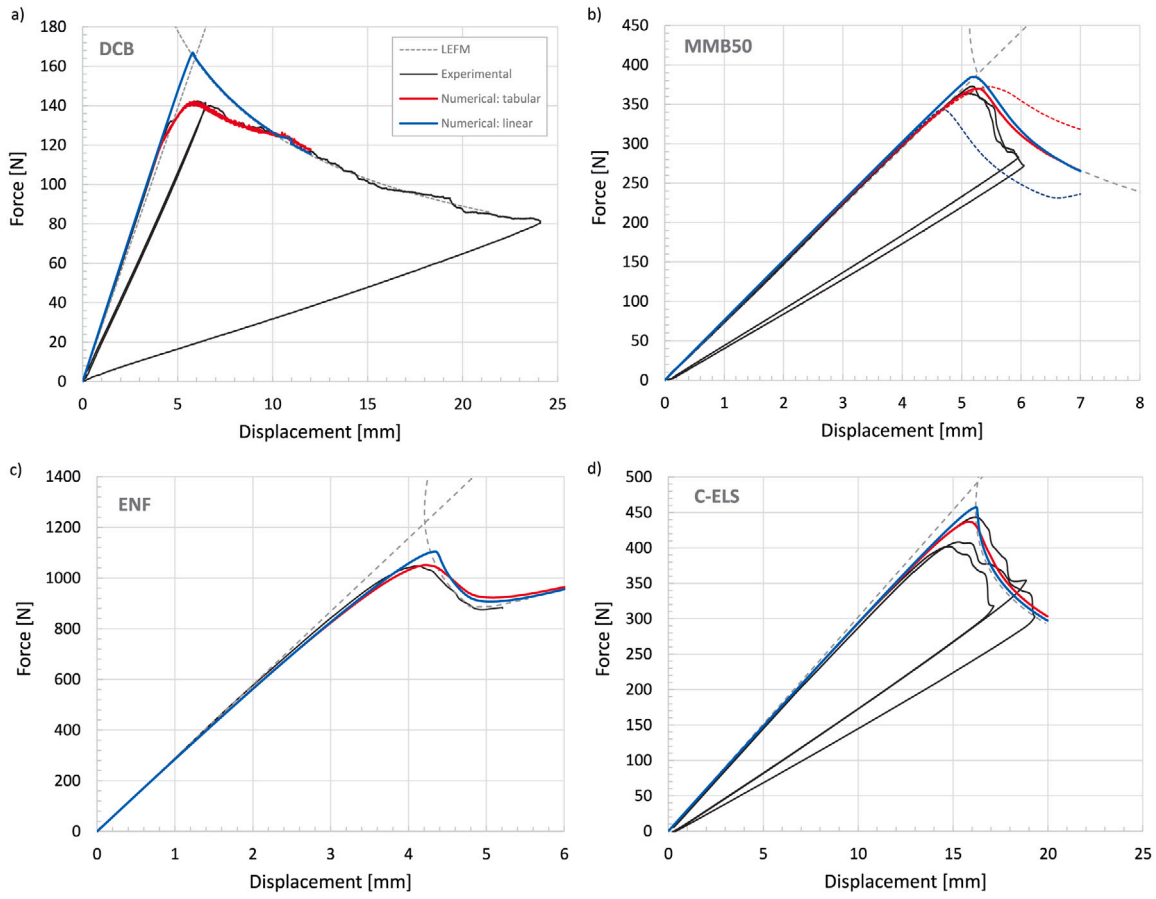

Fig. 25. Experimental versus numerical results: (a) Mode I — Double Cantilever Beam; (b) Mixed-Mode Bending 50%, dotted line excluding B = 0.1 cohesive law; (c) Mode II — End-Notched Flexure; (d) Mode II — Calibrated End Loaded Split.

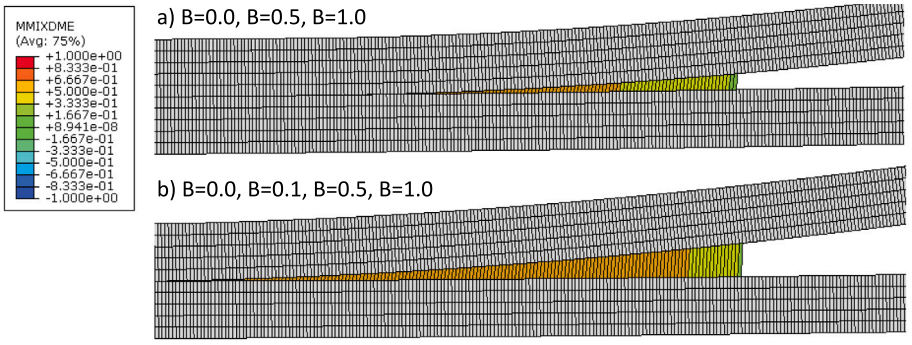

Fig. 26. Mixed-mode bending 50%, mode mixity in fracture process zone: (a) Tabular cohesive law excluding B = 0.1; (b) Tabular cohesive law including B = 0.1;.

5. Conclusions

The interlaminar behavior of AS4D/PEKK-FC thermoplastic composites is characterized and analyzed during quasi-static loading, while considering fiber bridging and R-curve effects. Mode I, II and Mixed Mode I/II at 50:50 experimental tests and numerical analyses are performed on the Double Cantilever Beam, End-Notched Flexure, Calibrated End Loaded Split and Mixed-Mode Bending 50% test configurations. Mode II testing with the End-Notched Flexure test method appeared to be difficult due to the large fracture process zone, but this could be adjusted for by using a larger span and a different initial crack length. Scanning electron microscopy is performed to provide new insights into the interlaminar damage mechanisms present in this large fracture process zone. The SEM micrographs confirmed the presence of large scale fiber bridging and significant plastic deformation is observed in the thermoplastic polymer matrix. The SEM micrographs also confirmed the absence of fiber bridging in Mixed Mode I/II at 50:50 and Mode II loading conditions and suggests that polymer crystallization plays and important role in the matrix-dominated behavior. A new data reduction approach based on only the load–displacement is validated on thermoplastic composites. This approach provides a convenient way of evaluating the experimental data, especially when it is difficult to accurately monitor the crack tip experimentally due to the large fracture process zone. By using this new approach it is also found that the cohesive laws of the Mode II tests were nearly identical, which confirms that the cohesive law is indeed independent of the test configuration. It is also shown that, even though both mode I and II tests were performed in different labs with different testing methods, reproducible results are obtained. Furthermore, a new procedure is developed to implement user-defined cohesive laws in commercial finite element

software, without the need for user-subroutines. The procedure ensures an accurate solution, even when a high penalty stiffness and/or rapid changes in shape of the cohesive law are present. The use of these new methods also provides new insights into the role of fiber bridging on the mixed-mode interlaminar behavior. Especially in mode I, a large influences in the fracture toughness is found, while the initiation fracture toughness is found to be rather low. As fiber bridging is not present during all mode I tests, it is considered to be a likely source of scatter in the propagation fracture toughness. It is also found that fiber bridging only contributed when sufficient crack opening is present. This makes accounting for the full cohesive law important, especially for small cracks that do not benefit from this increased mechanical property. Mixed Mode I/II at 50:50 and Mode II loading conditions also showed low initiation fracture toughness values. However, the initiation strength values from the experimental cohesive laws were found the be in line with the low shear initiation strength measured during during cycle in-plane shear loading from literature. The means the shear initiation strength is close to the 0.2% or 0.5% off-set shear strength. The resulting mixed-mode tabular cohesive laws are successfully implemented into a single material card for the numerical analysis and allows to obtain good correlation for all the different experimental test configurations.

CRediT authorship contribution statement

B.H.A.H. Tijs: Conceptualization, Methodology, Software, Investigation, Validation, Writing – original draft & editing. **S. Abdel-Monsef:** Software, Writing – reviewing. **J. Renart:** Conceptualization, Methodology, Investigation, Writing – reviewing. **A. Turon:** Supervision, Conceptualization, Writing – reviewing. **C. Bisagni:** Supervision, Conceptualization, Writing – reviewing.

Declaration of competing interest

The authors declare that they have no known competing financial interests or personal relationships that could have appeared to influence the work reported in this paper.

Data availability

Data will be made available on request.

Acknowledgments

The authors would like to thank the journal and editors for organizing this special issue in memory of our dear friend and colleague Claudio Lopes and are honored to participate. The first author would like to thank the AMADE testing facilities of the University of Girona and the DASML lab at Delft University of Technology for their support during the testing campaign. The work described in this paper received co-funding from the Clean Sky 2 Joint Undertaking (JU) under grant agreement No 945583 (project STUNNING). The JU receives support from the European Union's Horizon 2020 research and innovation programme and the Clean Sky 2 JU members other than the Union.

Disclaimer

The results, opinions, conclusions, etc. presented in this work are those of the author(s) only and do not necessarily represent the position of the JU; the JU is not responsible for any use made of the information contained herein.

References

[1] van Ingen JW, Waleson JEA, Offringa A, Chapman M. Double curved thermoplastic orthogrid rear fuselage shell. In: SAMPE Europe conference. Nantes, France; 2019, p. 1–10.

[2] Tijs BHAH, van Dooren KS, Bisagni C. Development of a numerical framework for virtual testing to support design of a next generation thermoplastic multifunctional fuselage. In: European conference on multifunctional structures (EMuS2020), November, 17-18, 202. Scipedia, S.L.; 2020, p. 90–5. http://dx.doi.org/10.23967/EMUS.2020.005.

[3] Solvay. Technical data sheet: APC (PEKK-FC) PEKK-FC thermoplastic polymer prepreg. 2017, URL: https://catalogservice.solvay.com/downloadDocument?fileId=MDkwMTY2OWM4MDU0YjY0OQ==&fileName=APC-PEKK-FC_CM_EN.pdf&base=FAST.

[4] Carlsson LA, Gillespie JW, Trethewey BR. Mode II Interlaminar Fracture of Graphite/Epoxy and Graphite/PEEK:. 5 (3), 1986, 170–187. http://dx.doi.org/10.1177/073168448600500302.

[5] Moore DR. Toughness characterization of carbon fibre/polyether ether ketone (CF/PEEK) laminates. Pure Appl Chem 1991;63(11):1609–25. http://dx.doi.org/10.1351/PAC199163111609/MACHINEREADABLECITATION/RIS.

[6] Wang H, Vu-Khanh T. Use of end-loaded-split (ELS) test to study stable fracture behaviour of composites under mode II loading. Compos Struct 1996;36(1–2):71–9. http://dx.doi.org/10.1016/S0263-8223(96)00066-9.

[7] Turon A, Camanho PP, Costa J, Dávila CG. A damage model for the simulation of delamination in advanced composites under variable-mode loading. Mech Mater 2006;38(11):1072–89. http://dx.doi.org/10.1016/J.MECHMAT.2005.10.003.

[8] Reeder JR, Crews JH. Mixed-mode bending method for delamination testing. AIAA J 2012;28(7):1270–6. http://dx.doi.org/10.2514/3.25204.

[9] Sacchetti F, Grouve WJ, Warnet LL, Villegas IF. Effect of resin-rich bond line thickness and fibre migration on the toughness of unidirectional carbon/PEEK joints. Composites A 2018;109:197–206. http://dx.doi.org/10.1016/j.compositesa.2018.02.035.

[10] Hojjati M, Chen J, Yousefpour A, Pratte J. Crystallization kinetics of cypek^{TM} poly ether ketone ketone. In: International SAMPE symposium and exhibition (proceedings), Vol. 52. 2008.

[11] Gardner KCH, Hsiao BS, Matheson RR, Wood BA. Structure, crystallization and morphology of poly (aryl ether ketone ketone). Polymer 1992;33(12):2483–95. http://dx.doi.org/10.1016/0032-3861(92)91128-O.

[12] Tan W, Falzon BG, Price M. Predicting the crushing behaviour of composite material using high-fidelity finite element modelling. Int J Crashworthiness 2015;20(1):60–77. http://dx.doi.org/10.1080/13588265.2014.972122.

[13] Vankan WJ, Tijs BHAH, De Jong GJ, De Frel HC, Singh NK. Strength of notched and un-notched thermoplastic composite laminate in biaxial tension and compression. J Compos Mater 2016;50(25). http://dx.doi.org/10.1177/0021998315621963.

[14] Baran I, Warnet LL, Akkerman R. Assessment of failure and cohesive zone length in co-consolidated hybrid C/PEKK butt joint. Eng Struct 2018;168:420–30. http://dx.doi.org/10.1016/J.ENGSTRUCT.2018.04.089.

[15] Tijs BHAH, Doldersum MHJ, Turon A, Waleson JEA, Bisagni C. Experimental and numerical evaluation of conduction welded thermoplastic composite joints. Compos Struct 2022;281:114964. http://dx.doi.org/10.1016/J.COMPSTRUCT.2021.114964.

[16] Tvergaard V, Hutchinson JW. The relation between crack growth resistance and fracture process parameters in elastic-plastic solids. J Mech Phys Solids 1992;40(6):1377–97. http://dx.doi.org/10.1016/0022-5096(92)90020-3.

[17] Sørensen BF, Jacobsen TK. Large-scale bridging in composites: R-curves and bridging laws. Composites A 1998;29(11):1443–51. http://dx.doi.org/10.1016/S1359-835X(98)00025-6.

[18] Sarrado C, Turon A, Costa J, Renart J. An experimental analysis of the fracture behavior of composite bonded joints in terms of cohesive laws. Composites A 2016;90:234–42. http://dx.doi.org/10.1016/J.COMPOSITESA.2016.07.004.

[19] de Moura MF, de Morais AB. Equivalent crack based analyses of ENF and ELS tests. Eng Fract Mech 2008;75(9):2584–96. http://dx.doi.org/10.1016/J.ENGFRACMECH.2007.03.005.

[20] Turon A, González EV, Sarrado C, Guillamet G, Maimí P. Accurate simulation of delamination under mixed-mode loading using a cohesive model with a mode-dependent penalty stiffness. Compos Struct 2018;184:506–11. http://dx.doi.org/10.1016/j.compstruct.2017.10.017.

[21] Campilho RD, Banea MD, Neto JA, Da Silva LF. Modelling adhesive joints with cohesive zone models: effect of the cohesive law shape of the adhesive layer. Int J Adhes Adhes 2013;44:48–56. http://dx.doi.org/10.1016/J.IJADHADH.2013.02.006.

[22] Jensen SM, Martos MJ, Bak BL, Lindgaard E. Formulation of a mixed-mode multilinear cohesive zone law in an interface finite element for modelling delamination with R-curve effects. Compos Struct 2019;216:477–86. http://dx.doi.org/10.1016/J.COMPSTRUCT.2019.02.029.

[23] Dávila CG, Rose CA, Camanho PP. A procedure for superposing linear cohesive laws to represent multiple damage mechanisms in the fracture of composites. Int J Fract 2009;158(2):211–23. http://dx.doi.org/10.1007/S10704-009-9366-Z, 2009, 158 (2).

[24] Tamuzs V, Tarasovs S, Vilks U. Progressive delamination and fiber bridging modeling in double cantilever beam composite specimens. Eng Fract Mech 2001;68(5):513–25. http://dx.doi.org/10.1016/S0013-7944(00)00131-4.
[25] Yin S, Gong Y, Li W, Zhao L, Zhang J, Hu N. A novel four-linear cohesive law for the delamination simulation in composite DCB laminates. Composites B 2020;180:107526. http://dx.doi.org/10.1016/J.COMPOSITESB.2019.107526.
[26] Raimondo A, Urcelay Oca I, Bisagni C. Influence of interface ply orientation on delamination growth in composite laminates. J Compos Mater 2021;55(27):3955–72. http://dx.doi.org/10.1177/00219983211031636.
[27] Sørensen BF, Jacobsen TK. Characterizing delamination of fibre composites by mixed mode cohesive laws. Compos Sci Technol 2009;69(3–4):445–56. http://dx.doi.org/10.1016/J.COMPSCITECH.2008.11.025.
[28] ASTM D5528-13, standard test method for mode I interlaminar fracture toughness of unidirectional fiber-reinforced polymer matrix composites. West Conshohocken, PA: ASTM International; 2013.
[29] ASTM D7905 / D7905M-19e1, standard test method for determination of the mode II interlaminar fracture toughness of unidirectional fiber-reinforced polymer matrix composites. West Conshohocken, PA: ASTM International; 2019.
[30] ISO 15114:2014 Fibre-reinforced plastic composites — Determination of the mode II fracture resistance for unidirectionally reinforced materials using the calibrated end-loaded split (c-ELS) test and an effective crack length approach. 2014.
[31] ASTM D6671 / D6671M-19, standard test method for mixed mode I-Mode II interlaminar fracture toughness of unidirectional fiber reinforced polymer matrix composites. West Conshohocken, PA: ASTM International; 2019.
[32] Abdel Monsef S, Ortega A, Turon A, Maimí P, Renart J. An efficient method to extract a mode I cohesive law for bonded joints using the double cantilever beam test. Composites B 2019;178:107424. http://dx.doi.org/10.1016/j.compositesb.2019.107424.
[33] Abdel Monsef S, Pérez-Galmés M, Renart J, Turon A, Maimí P. The influence of mode II test configuration on the cohesive law of bonded joints. Compos Struct 2020;234:111689. http://dx.doi.org/10.1016/j.compstruct.2019.111689.
[34] ISO 15024:2001 Fibre-reinforced plastic composites — Determination of mode I interlaminar fracture toughness, GIC, for unidirectionally reinforced materials. 2001.
[35] Renart J, Blanco N, Pajares E, Costa J, Lazcano S, Santacruz G. Side clamped beam (SCB) hinge system for delamination tests in beam-type composite specimens. Compos Sci Technol 2011;71(8). http://dx.doi.org/10.1016/j.compscitech.2010.10.005.
[36] Hashemi S, Kinloch A, Williams J. The analysis of interlaminar fracture in uniaxial fibre-polymer composites. Proc R Soc Lond Ser A Math Phys Eng Sci 1990;427(1872):173–99. http://dx.doi.org/10.1098/RSPA.1990.0007.
[37] Barrett JD, Foschi RO. Mode II stress-intensity factors for cracked wood beams. Eng Fract Mech 1977;9(2):371–8. http://dx.doi.org/10.1016/0013-7944(77)90029-7.
[38] Wang Y, Williams JG. Corrections for mode II fracture toughness specimens of composites materials. Compos Sci Technol 1992;43(3):251–6. http://dx.doi.org/10.1016/0266-3538(92)90096-L.
[39] Turon A, Camanho PP, Costa J, Renart J. Accurate simulation of delamination growth under mixed-mode loading using cohesive elements: Definition of interlaminar strengths and elastic stiffness. Compos Struct 2010;92(8):1857–64. http://dx.doi.org/10.1016/j.compstruct.2010.01.012.
[40] Tvergaard V, Hutchinson JW. The influence of plasticity on mixed mode interface toughness. J Mech Phys Solids 1993;41(6):1119–35. http://dx.doi.org/10.1016/0022-5096(93)90057-M.
[41] Ortega A, Maimí P, González EV, Trias D. Characterization of the translaminar fracture Cohesive Law. Composites A 2016;91:501–9. http://dx.doi.org/10.1016/J.COMPOSITESA.2016.01.019.
[42] Abdel-Monsef S, Renart J, Carreras L, Maimí P, Turon A. Environmental effects on the cohesive laws of the composite bonded joints. Composites A 2022;155:106798. http://dx.doi.org/10.1016/J.COMPOSITESA.2021.106798.
[43] Bouvet C, Serra J, Perez PG. Strain rate effect of mode II interlaminar fracture toughness on the impact response of a thermoplastic PEEK composite. Composites C 2020;2:100031. http://dx.doi.org/10.1016/J.JCOMC.2020.100031.
[44] Benzeggagh ML, Kenane M. Measurement of mixed-mode delamination fracture toughness of unidirectional glass/epoxy composites with mixed-mode bending apparatus. Compos Sci Technol 1996;56(4):439–49. http://dx.doi.org/10.1016/0266-3538(96)00005-X.
[45] Pérez-Martín H, Mackenzie P, Baidak A, Ó Brádaigh CM, Ray D. Crystallinity studies of PEKK and carbon fibre/PEKK composites: A review. Composites B 2021;223:109127. http://dx.doi.org/10.1016/J.COMPOSITESB.2021.109127.
[46] Turon A, Dávila CG, Camanho PP, Costa J. An engineering solution for mesh size effects in the simulation of delamination using cohesive zone models. Eng Fract Mech 2007;74(10):1665–82. http://dx.doi.org/10.1016/j.engfracmech.2006.08.025.
[47] Van Paepegem W, De Baere I, Degrieck J. Modelling the nonlinear shear stress–strain response of glass fibre-reinforced composites. Part I: Experimental results. Compos Sci Technol 2006;66(10):1455–64. http://dx.doi.org/10.1016/J.COMPSCITECH.2005.04.014.